Oxygen vacancy-induced spin polarization of tungsten oxide nanowires for efficient photocatalytic reduction and immobilization of uranium(VI) under simulated solar light

Xudong Yang [a,b,c,d], Fan Li [b], Wen Liu [a,b,*], Long Chen [b], Juanjuan Qi [c,d], Weiliang Sun [e], Fei Pan [a,**], Tao Duan [f], Fengbin Sun [g,**]

[a] *School of Environmental Engineering, Wuhan Textile University, Engineering Research Centre for Clean Production of Textile Dyeing and Printing, Ministry of Education, Wuhan 430073, China*
[b] *College of Environmental Sciences and Engineering, The Key Laboratory of Water and Sediment Sciences (Ministry of Education), Peking University, Beijing 100871, China*
[c] *College of Environmental Science and Engineering, North China Electric Power University, Beijing 102206, China*
[d] *The Key Laboratory of Resources and Environmental System Optimization, Ministry of Education, North China Electric Power University, Beijing 102206, China*
[e] *Department of Civil and Environmental Engineering, Louisiana State University, Baton Rouge 70803, LA, USA*
[f] *State Key Laboratory of Environment-friendly Energy Materials, Southwest University of Science and Technology, Mianyang 621010, Sichuan, China*
[g] *Institute of Urban Meteorology, China Meteorological Administration, Beijing 100089, China*

ARTICLE INFO

ABSTRACT

Tungsten oxide nanowires (WO_{3-x}) with rich oxygen vacancies (OVs) were fabricated through a facile hydrothermal method, which had both high adsorptive capability and photocatalytic activity. 95.1% of total U(VI) (C_0 = 10 mg/L) was removed by WO_{3-x} at pH 5, and 79.9% was transformed to U(IV) to achieve reductive immobilization after photocatalysis under simulated solar light. Band structure and optical characterizations indicated WO_{3-x} had narrower band gap energy, but higher charger carrier separation and transfer rates compared with conventional WO_3. Density functional theory (DFT) calculations further demonstrate the spin polarization state electrons of W 5d in WO_{3-x} due to the construction of OVs, thus greatly inhibiting recombination of electron-hole pairs. In addition, the electron density increases in WO_{3-x} and the photogenerated e^- in the conduction band of WO_{3-x} has higher reduction ability than WO_3, leading to more efficient electron transfer from WO_{3-x} to UO_2^{2+} after photo-excitation for U(VI) reduction.

1. Introduction

Radioactive wastewater containing uranium (U) will pose severe environmental and health risks if not well treated due to its high radioactivity and carcinogenic effect [1,2]. U(VI) in the form of uranyl cation (UO_2^{2+}) with high mobility and solubility is the main species in water [3]. Uranium mining and unintentionally nuclear safety accidents aggravate U(VI) migration and pollution in water environment [4]. According to the regulation of World Health Organization (WHO), the U concentration should be lower than 30 μg/L for discharging wastewater [5], however, excessive U concentration has been frequently reported around the world [5,6]. Therefore, U(VI) removal in water/wastewater

has become increasingly important and urgent.

For removal of U(VI) in water, the technologies of ion exchange, adsorption [7] and membrane separation [8] usually possess distinct disadvantages like high energy consumption, non-detoxification process and potential secondary pollution. Therefore, the most effective strategy for removal of U(VI) in water proceeds as initial reduction and subsequent immobilization/adsorption [9], as U(IV) in the form of UO_2 (s) is less toxic and exhibits lower mobility than UO_2^{2+} [3]. However, it is difficult to achieve transformation of mobile U(VI) to immobile U(VI) under normal conditions because of the low redox potential (0.411 V) in terms of UO_2^{2+}/UO_2 [10]. The chemical reduction method using reducing agents or materials may also lead to high cost and unexpected

---

secondary pollution [11]. Recently, photocatalysis shows great application potential to U(VI) reduction because of the advantages including efficient utilization of green energy, detoxification process, low cost and low secondary pollution potential [12,13]. High-efficient photocatalysts are the key of photocatalysis for U(VI) reduction. Previously, various photocatalysts such as niobite/titanate nanoflakes heterojunction (Nb/TiNFs) [3], WO_3/g-C_3N_4 [14], $ZnFe_2O_4$ nanorods [12], 3D defect-rich Ti_2CT_x-MXene-derived TiO_2 @ reduced graphene oxide (TiO_2(M)@RGO) [15] and Ti_3C_2/$SrTiO_3$ [16] have been developed to achieve photocatalytic reduction of U(VI). However, considering easy remobilization and re-oxidation of U(IV) even under conventional environmental conditions [17], novel photocatalysts for U removal should be designed with both high photocatalytic activity and good adsorption performance, thus achieving simultaneous photocatalytic reduction of U(VI) and immobilization of U(IV).

Vacancies construction is widely proposed to promote the photocatalytic activity of photocatalysts. Specifically, oxygen vacancies (OVs) can affect the e^- structural properties and the production of cation disorder, thus further inhibiting the recombination of e^-–h^+ and improving the photocatalytic efficiency [18]. Meanwhile, OVs in the transition metal semiconductors also can regulate the spin polarization of the space near the Fermi surface of material, thus enhancing the non-uniform distribution of the material's charge and the density of the state (DOS) near the Fermi surface. Besides, after OVs construction, the d-band center energy level of the transition metal (such as W) increases, exhibiting improved adsorption capacity of target pollutant (*e.g.*, UO_2^{2+}) [19]. Tungsten oxide (WO_3), as a low-cost and environmental-friendly photocatalyst, has specific optical properties, band structures (~2.8 eV), stable chemical performance and low toxicity, which is widely applied in the environmental photocatalysis area such as pollutants degradation and CO_2 reduction [20]. Meanwhile, WO_3 can maintain its original crystal structure in radioactive wastewater owing to the strong scattering of γ-ray *via* W atoms, thus suggesting WO_3 is a potential catalyst towards the treatment of radionuclides in water [6]. In addition, WO_3 also has high charge carrier transfer properties after photo-excitation [21,22]. Compared with other metal semiconductors, WO_3 can easily be tailored for construction of OVs in the crystal lattice, and then its light absorption can be greatly extended even to the near-infrared region (NIR), achieving effective utilization of solar light [23]. Moreover, OVs in WO_3 also can facilitate the adsorption capability of reactants (such as UO_2^{2+}) [24]. Thus, construction of OVs in WO_3 can greatly promote its photocatalytic and adsorptive properties, while few studies reported photocatalytic removal of U(VI) by WO_3 with OVs. Moreover, the role of OVs and underlying mechanism of enhanced photocatalytic activity also need to be revealed.

In this work, WO_3 nanowires with OVs (labeled as WO_{3-x}) were synthesized through a facile solvothermal method, which was applied for photocatalytic reduction and immobilization of U(VI) under simulated solar light. The specific objectives of this work were: (1) to explore the composition, crystal structure and band structure of WO_{3-x}; (2) to test the ability of WO_{3-x} to remove U(VI) including adsorption and photocatalytic reduction; (3) to evaluate the effects of water chemical factors (pH, co-existing ions, typical natural organic matter (NOM)) on U(VI) removal; (4) to explore the specific role of OVs by density-functional theory (DFT) calculations, and to verify superior electronic structure and adsorption energy of WO_{3-x}; (5) to reveal the mechanism of U(VI) removal by WO_{3-x} under solar light. Overall, this work can provide useful information on OVs-based photocatalysts developing for efficient U(VI) removal in water, which is of great significance for treatment of radioactive contaminated water.

2. Experimental section

2.1. Chemicals and catalysts synthesis

All chemicals used in this study were analytical reagent (AR) or

higher. $UO_2(NO_3)_2 \cdot 6 H_2O$ was served as the U(VI) source. The information on chemicals are shown in Text S1 of Supplementary Data **(SD)**. The WO_{3-x} was synthesized by a facile hydrothermal method modified by previous studies [25]. Firstly, 0.1 g WCl_6 was dissolved into ethanol (EtOH, 66 mL) and fully stirred to obtain a transparent yellow solution. Then, the solution was put into a Teflon-lined stainless autoclave and hydrothermally treated at 180 °C for 12 h. After the reactor was cooled down, blue products were acquired after centrifugation (8000 rpm, 5 min) and washed with ethanol for 3 times. Finally, WO_{3-x} materials were obtained after oven-dried at 80 °C for 6 h. In addition, WO_3 without oxygen vacancy was also synthesized through calcination of WO_{3-x} in a muffle furnace at 500 °C for 2 h in air. In comparison, a WO_{3-x} material with low OVs concentration (labeled as L-WO_{3-x}) was also synthesized through the same method while hydrothermally treated at a lower temperature of 160 °C) [26].

Material characterization methods are presented in Text S2, including scanning electron microscopy (SEM), transmission electron microscopy (TEM), high-resolution TEM (HRTEM), energy dispersive spectra (EDS), X-ray diffraction (XRD), X-ray photoelectron spectroscopy (XPS), Brunauer-Emmett-Teller (BET) specific surface area analysis, Fourier transform infrared spectrometer (FT-IR), diffuse reflectance UV–vis absorption spectra (UV–vis DRS), photoluminescence spectra (PL), time resolution photoluminescence spectra (TR-PL), zeta potential analysis and magnetization (M-H) curves analysis. Besides, Text S3 presents the methods on electron paramagnetic resonance (EPR) analysis, including materials (solid) detection and radicals identification in solution.

2.2. The photoelectrical properties of materials

The photoelectrical properties of WO_3 and WO_{3-x} were measured on electrochemical workstation (CHI660, China) equipped with PEC2000 light (Beijing Perfectlight Technology Co., Ltd. China), and the detailed information is described in Text S4.

2.3. Uranium removal experiments and analytical methods

To test the adsorption performance of U(VI) by materials, all the batch adsorption experiments were carried out in polyethylene bottles in dark. The solution pH was adjusted by diluted HNO_3 and NaOH (0.1 mM). For adsorption kinetics, 0.2 g/L of material was added into U(VI) solution (initial concentration = 100 mg/L) at pH 5, and the adsorption process was maintained for 360 min. For adsorption isotherms, 0.2 g/L of material was added into U(VI) solution with initial concentrations varying from 10 to 200 mg/L at pH 5. For pH effect, the solution pH was adjusted to 3–11. After adsorption, samples were immediately filtered through 0.22 μm polyethersulfone (PES) membrane to obtain residual U(VI) solution for further detection. Control tests suggested that there was almost no U(VI) loss (<1%) for adsorption by bottle and membrane only. The adsorption results were also analyzed using adsorption kinetics and isotherms models, which are described in Text S5 in detail.

To test the photocatalytic activity of materials for U(VI) reduction, experiments were conducted in a quartz reactor (total volume = 250 mL) with circulating water injected to maintain the reaction temperature of 25 ± 0.2 °C. A Xenon light (300 W, PLS-SXE300D, Beijing Perfectlight Technology Co., Ltd. China) was applied to simulate solar light at 1.5 G mode with the light intensity of 80 ± 5 mW/cm^2. In a typical photocatalysis reaction, 0.2 g/L material was added in 10 mg/L U(VI) solution at pH 5. After reaction, the sample was conducted a classical carbonate (CARB) extraction to quantify the U(VI) content on the material [27]. Specifically, 10 mL $NaHCO_3$ (14.4 mM) and Na_2CO_3 (2.8 mM) miscible liquids were mixed with 10 mL sample, and then fully stirred for 1 h to complete the extraction. Finally, the U(VI) concentration in the extracting solution was determined after filtration by 0.22 μm PES membrane. The U(VI) concentration in solution was measured using an inductively coupled plasma optical emission spectrometry (ICP-OES,

ICAP PRO, Thermofisher, USA) with a detection limit of 0.1 mg/L for U. To verify the impact of pH, the photo-reduction experiments also were conducted at pH 3–11. Meanwhile, ultraviolet (UV) cut-off and NIR cut-off filter (Beijing Perfectlight Technology Co., Ltd. China) were used to remove lights with wavelength < 420 nm and < 800 nm to evaluate the role of different lights to the U(VI) photo-reduction, respectively. In addition, magnets were used to investigate the effect of applied magnetic field (4–12 mT) for U(VI) removal in the photocatalysis system, which were placed close to the reactor (1 cm away). Meanwhile, the intensity of magnetic field was measured by a digital tesla meter (VC862A, Shenzhen Yisheng Victor Tech Co., Ltd, China).

In addition, to test the effect of co-existing ions and NOM, 5 mM ions like HCO_3^-, CO_3^{2-}, Ca^{2+}, Na^+ and HA (5 mg/L as total organic carbon) were added into the reaction system, respectively. To evaluate the reusability of WO_{3-x}, the catalyst was gathered by 0.22 μm PES membrane after the first experiment on U(VI) photocatalysis. Subsequently, the next removal test was consistent with the first experiment and proceeded five cycles under the same conditions. The leaching of W ions in the five reuse cycles was also measured by using ICP-OES.

2.4. DFT calculations

The band and electronic structures, density of state (DOS), partial density of state (PDOS), adsorption energy, electron density difference (EDD), work function and electron density were calculated by Cambridge Sequential Total Energy Package (CASTEP) on Materials Studio 2020 with plane-wave-based pseudo potential method according to DFT [28]. Text S7 describes the detailed information on DFT calculations.

3. Results and discussion

3.1. The morphologies and crystal phases of WO_{3-x} nanowires and WO_3 nanorods
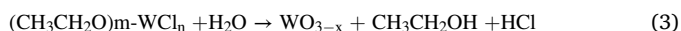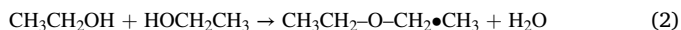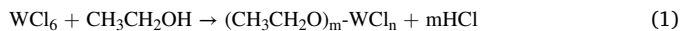
Fig. 1a presents the schematic diagram on formation of WO_{3-x} in the solvothermal process (180 °C for 12 h). EtOH was not only applied as solvent for the reaction, but also acted as a reducing agent for OVs formation. For the mechanism on OVs formation in tungsten oxide through hydrothermal process, the WCl_6 precursor firstly reacted with CH_3CH_2OH to generate HCl and $(CH_3CH_2O)_m$-WCl_n (Eq. (1)). Then, H_2O was generated *via* condensation reaction between two CH_3CH_2OH molecules in the solvothermal process (Eq. (2)). Finally, the $(CH_3CH_2O)_m$-WCl_n further reacted with H_2O to generate WO_{3-x} with OVs (Eq. (3)) [29,30]. Then, WO_3 without OVs can be obtained through calcination of WO_{3-x} in air (500 °C for 2 h) [31]. The SEM (Fig. 1b) and TEM (Fig. 1c) images both show that WO_{3-x} possessed nanowires morphology with homogeneous one-dimensional (1D) structures, with diameters of 10–30 nm (Fig. 1d) and lengths of > 1000 nm (Fig. 1c). In
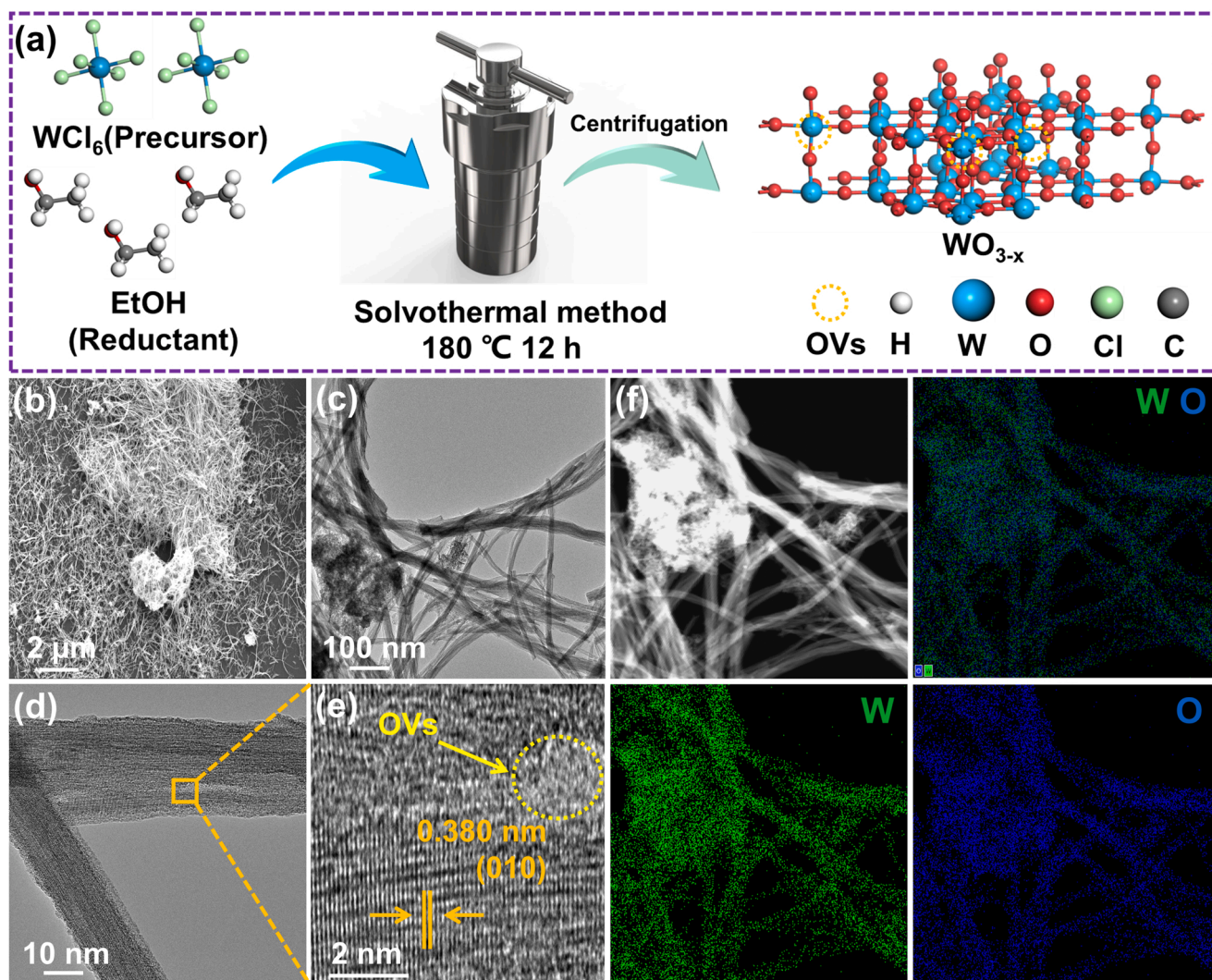
Fig. 1. (a) The schematic diagram on preparation process of WO_{3-x}; (b) SEM image of WO_{3-x}; (c) TEM image of WO_{3-x}; (d) and (e) HRTEM images of WO_{3-x}; (f) TEM-EDS elemental mapping of WO_{3-x}.

addition, the lattice fringe space distance of WO_{3-x} was determined to be 0.380 nm (Fig. 1e), assigned to the (010) lattice plane of monoclinic $W_{18}O_{49}$ ($WO_{2.72}$, JCPDS No. 71–2450) [32]. Besides, obvious defect sites were observed in HRTEM (Fig. 1e), indicating OVs were successfully construed in WO_{3-x} [33]. The TEM-EDS elemental mapping (Fig. 1f) clearly displays that W and O were evenly dispersed in WO_{3-x}. In comparison, the as-synthesized WO_3 exhibited nanorods morphology based on SEM and TEM images (Fig. S1a-c), which was quite different from that of WO_{3-x}. Then, Fig. S1d shows a clear lattice spacing of 0.382 nm, corresponded to the exposed (001) lattice plane of monoclinic WO_3 (JCPDS No. 43–1035) [31]. Meanwhile, the TEM-EDS mapping results also verified the existence of W and O in the WO_3 nanorods (Fig. S1e).

$$WCl_6 + CH_3CH_2OH \rightarrow (CH_3CH_2O)_m\text{-}WCl_n + mHCl \quad (1)$$

$$CH_3CH_2OH + HOCH_2CH_3 \rightarrow CH_3CH_2\text{-}O\text{-}CH_2\bullet CH_3 + H_2O \quad (2)$$

$$(CH_3CH_2O)m\text{-}WCl_n + H_2O \rightarrow WO_{3-x} + CH_3CH_2OH + HCl \quad (3)$$

The BET surface area and pore volume and pore size distributions of WO_{3-x} nanowires and WO_3 nanorods were further analyzed (Fig. S2). The two materials showed type IV isotherms with an apparent H_3 hysteresis loop under the relative pressures from 0.8 to 1.0 P/P_0 (Fig. S2a and c) [34], suggesting the existence of porous structure (slit-like pores, 2–50 nm) [35]. Besides, the BET surface area of WO_{3-x} (123.6 m^2/g) was much larger than that of WO_3 (18.6 m^2/g), due to the formation of porous nanowires structure with OVs [36]. The BJH pore volume distribution results further confirmed that WO_{3-x} had a much higher total pore volume of 0.35 cm^3/g than WO_3 (0.14 cm^3/g). Moreover, smaller pores centered at ~2 and ~4 nm were observed in WO_{3-x}, attributed to OVs-induced pores, while the pores of WO_3 mainly located at ~20 nm (Fig. S2b and d).

The crystalline phase of WO_{3-x} and WO_3 were studied by XRD (Fig. 2a). For WO_3 nanorods, all the diffraction peaks well matched with monoclinic WO_3 (JCPDS No. 43–1035) [31]. However, WO_{3-x} nanowires mainly displayed two diffraction peaks at 23.08° and 47.27°, assigned to the (010) and (020) crystalline planes of monoclinic $WO_{2.72}$ (JCPDS No. 71–2450) respectively, suggesting that nonstoichiometric

WO_3 with rich OVs was formed. The sharp peak at 23.08° also indicated that WO_{3-x} largely exposed (010) lattice plane, which is in accordance with the TEM result (Fig. 1e). For WO_{3-x} synthesized at 180 °C, the material primarily grew along (010) lattice plane, so the other lattice planes could be hardly observed. Meanwhile, the other diffraction peaks of WO_{3-x} could not be obviously identified, because the existence of OVs would impede the crystallization of WO_{3-x} [37]. In addition, no other intensity diffraction peaks were found, indicating the crystallization for formation of WO_{3-x} nanowires grew along (010) plane. In the FT-IR spectra (Fig. 2b), the peaks assigned to O–H and H–O–H stretching (~3448 cm^{-1}) and bending vibration (~1616 and ~1406 cm^{-1}) on WO_3 and WO_{3-x} surface were found [38]. In addition, the contraction vibration at 500–1000 cm^{-1} was described as W–O bond [38]. Among them, the two vibrational bands at 580 and 659 cm^{-1} belonged to W–O–W stretching vibration [39]. The bands at 734 and 826 cm^{-1} were assigned to W=O and O–W–O stretching and bending vibration [38], respectively. Apparently, different FT-IR spectra of WO_{3-x} was observed compared with WO_3, indicating OVs in WO_{3-x} caused discrepancy for partial chemical bonds of material.

The element compositions and corresponding oxidation states of materials were obtained by XPS analysis. In the survey spectra of WO_{3-x} and WO_3 (Fig. 2c), the W 4 f and O 1 s photoelectron peaks could be clear observed. In the high-resolution spectra of W 4 f (Fig. 2d), the split peak of WO_3 at 35.5 eV was classified as W $f_{7/2}$ of W(VI) [40]. However, for WO_{3-x}, besides the W(VI) peak at 36.0 eV, another new peak at 34.7 eV attributed to W(V) appeared [41], indicating W(VI) was partially reduced and OVs were generated in WO_{3-x}. In addition, the W (VI) peak of WO_{3-x} also shifted to higher binding energy compared with that of WO_3, namely from 35.5 to 36.0 eV for W 4 $f_{7/2}$. It is suggested that the existence of OVs led to regulation of electron structure in WO_{3-x}, and the emergence of W(V) increased the electron density of W [42], which was beneficial to the e^- transportation and U(VI) reduction. In the high-resolution spectra of O 1 s (Fig. 2e), the two major peaks at 530.3 eV and 531.9 eV in WO_3 were assigned to the lattice oxygen (O_L) and adsorbed oxygen (O_A) from –OH group or H_2O, respectively [43]. However, WO_{3-x} possessed a new peak at 531.6 eV, which was indexed to the O of oxygen vacancies (O_V) [35]. Thus, XPS analysis also indicated

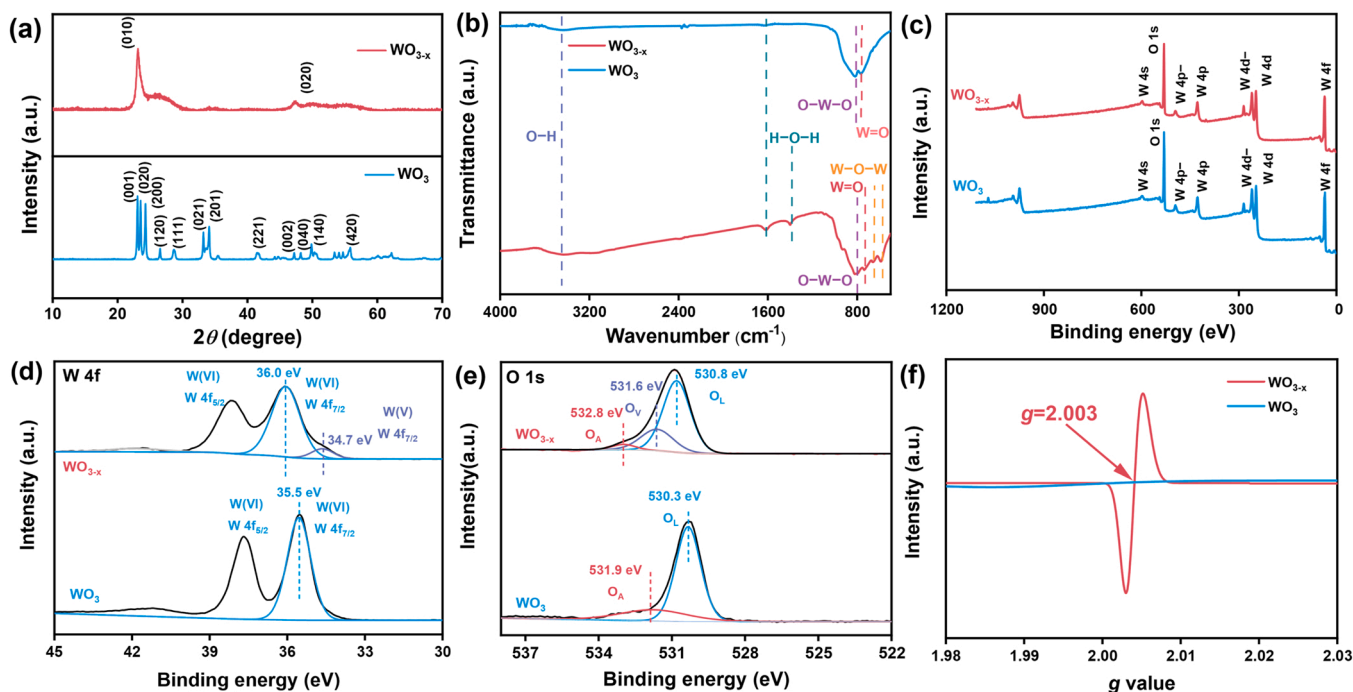**Fig. 2.** (a) XRD patterns and (b) FT-IR spectra of WO_{3-x} and WO_3; (c) the survey spectra of WO_{3-x} and WO_3; XPS high-resolution spectra of (d) W 4 f and (e) O 1 s of WO_{3-x} and WO_3 (f) the EPR detection of WO_{3-x} and WO_3.

the successful construction of OVs in WO_{3-x}, leading to accumulation of electrons on W for efficient photo-reduction of U(VI). EPR analysis further confirmed the existence of OVs in WO_{3-x} (Fig. 2f). It can be seen that WO_{3-x} presented an obvious signal at $g = 2.003$ in the EPR spectra, which was attributed to the signal of the single-electron-trapped (paramagnetic) OVs [10,44]. In comparison, WO_3 did not show any signal at $g = 2.003$ due to no OVs inside.

3.2. The band structures and photoelectric properties of WO_{3-x} and WO_3

The UV–vis DRS spectra show that WO_3 had a light absorption edge at 464 nm (insert figure of Fig. 3a). However, the light absorption edge of WO_{3-x} was extended to 488 nm, and WO_{3-x} exhibited much stronger light absorption capacity at > 400 nm. Thus, the photons capture ability of WO_{3-x} was dramatically increased in the visible light region

compared with WO_3 [13]. In addition, it is worth noting that WO_{3-x} displayed strong light absorption even in the NIR region at 750–1200 nm (Fig. 3a), which was retributed to the defective absorption stemmed from the existence of OVs. OVs could lead to the localized surface plasmon resonance (LSPR) effect. Specifically, if the oscillating frequencies of electrons and photons of metal well match, they will resonate at the interface between the dielectric and the metal, thus leading to an enhanced absorption of light (especially in NIR region) on the macroscale. Moreover, the improved absorption of light can generate more hot electrons and further promote the photocatalytic reaction [45]. The band energies (E_g) of WO_3 and WO_{3-x} were then calculated by Kubelka-Munk (K-M) transformation (Text S8) [13], which was 2.67 and 2.54 eV for WO_3 and WO_{3-x}, respectively (Fig. 3b). Therefore, the band gap of WO_{3-x} was narrowed after construction of OVs, as the absence of O atoms caused change of band energy structure,
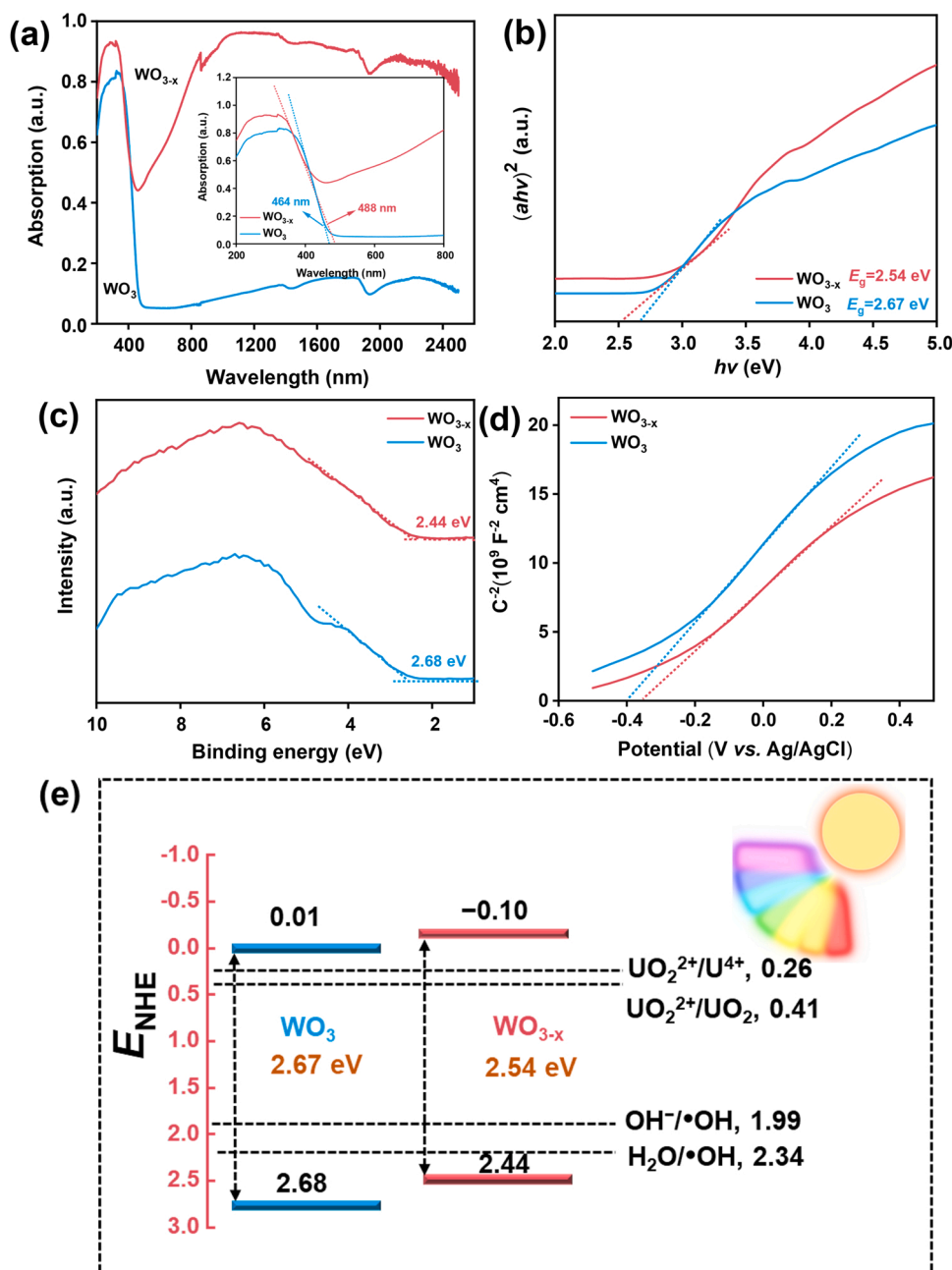
Fig. 3. (a) UV–vis DRS spectra, (b) band gap energy after Kubelka-Munk (K-M) transition, (c) VB-XPS spectra and (d) Mott-Schottky (M-S) plots of WO_3 and WO_{3-x}; (e) band structures of WO_{3-x} and WO_3.

and the valence band is generally contributed by O 2p orbitals for tungsten oxides [46], which will be discussed in detail in the next section. Besides, valence band XPS (VB-XPS) results showed that the VB energy was 2.44 and 2.68 eV for WO_{3-x} and WO_3 (Fig. 3c), respectively. Moreover, the Mott-Schottky (M-S) plots (Fig. 3d) results indicate the WO_{3-x} possessed smaller slope than WO_3, indicating it contains higher carrier concentration due to the construction of OVs [12,47]. Then, the CB energies of WO_3 and WO_{3-x} were also calculated, and the band structures of the two materials are shown in Fig. 3e.

To further illustrate the better photocatalytic properties of WO_{3-x} than WO_3, a series of photoelectric characterizations were conducted (Fig. 4 and Tables S1–S6). The lifetime of charge carrier was quantified by TR-PL (Fig. 4a and Table S6). WO_{3-x} had a shorter average lifetime (τ_{avg} = 78.35 ns) of charge carrier than that of WO_3 (99.13 ns), indicating more efficient charge carriers separation in WO_{3-x} [35,48]. Additionally, the electrochemical impedance spectroscopy (EIS) result revealed that WO_{3-x} with a smaller arc radius presented a lower resistance for charge transfer (Fig. 4b), and thus presented higher charge transfer efficiency [44]. Then, the PL spectra also indicate that WO_{3-x} exhibited a lower steady-state PL emission intensity compared with WO_3 (Fig. 4c), suggesting that WO_{3-x} had a lower recombination rate of photogenerated h^+–e^- pairs [35,44]. Fig. 4d displays the amperometric *i-t* curve (IT) curves of WO_{3-x} and WO_3 under simulated solar light. The photocurrent intensity of WO_{3-x} was much higher (~4 times) than that of WO_3, further demonstrating the higher efficiency of charge carrier transfer for WO_{3-x} with OVs [35]. Finally, the curves of cyclic voltammetry (CV) and linear sweep voltammetry (LSV) exhibit that WO_{3-x} presented a stronger current density and higher redox ability than WO_3, suggesting that the electrical conductivity and photocatalytic activity of WO_{3-x} were remarkably improved after OVs construction [49].

3.3. The electronic structures of WO_{3-x} and WO_3 analyzed by DFT calculations

To deeply reveal the enhanced photocatalytic activity of WO_{3-x} after OVs construction, the band structures, DOS spectra and electron density of materials were analyzed by DFT calculations (Fig. 5), and the relevant structural models of materials are shown in Fig. S3. It is indicated that WO_3 and WO_{3-x} are typical indirect band-gap semiconductors according to their band structures displayed in Fig. 5a and b. The calculated band gap (0.9 eV) of WO_{3-x} is much lower than that of WO_3 (1.92 eV). Meanwhile, the smaller band gaps are obtained than the experimental values, owing to the known limitation for plain DFT method [3]. In addition, a flat band appears at the conduction band minimum (CBM) for WO_{3-x} (Fig. 5b), attributed to the fact that W 5d electrons or W atoms are unpaired and excessive defects are generated. Therefore, a defect level below the CB in WO_{3-x} is formed based on the DFT analysis, enabling the electrons can more easily transfer to the defect level to reduce U(VI), thus improving the catalytic reactivity. In addition, the calculated band gap values of WO_3 and WO_{3-x} are smaller than the measured values (Fig. 3b), owing to the common limitation of the DFT method and underestimation of E_g for DFT calculation [50]. Thus, the narrowed gap and more dispersive CB of WO_{3-x} suggest the photoinduced e^- can be effectively migrated compared with WO_3, thus facilitating the photocatalytic reduction efficiency.

In the PDOS spectra (Fig. 5c and d), O 2p orbitals mainly contribute to the VB both for WO_3 and WO_{3-x}, while W 5d orbitals contribute to the CB. Meanwhile, the green region for WO_{3-x} is wider than that for WO_3, suggesting that WO_{3-x} has more O dangling bonds and the nonbonding electron of O atom in WO_{3-x} has higher energy [51,52], thus promoting the activity of electrons in W 5d band for catalytic reaction. In the DOS spectra (Fig. 5e and f), it can be seen that the CBM of WO_{3-x} moves to a low energy region compared with that of WO_3, indicating the electron density increases in WO_{3-x} and the photogenerated e^- in the CB of WO_{3-x} has higher reduction ability. In addition, the electron density state near the Fermi level also increases for WO_{3-x} (Fig. 5f), and the d-band center of WO_{3-x} shifts to − 0.05 eV compared with 1.97 eV of WO_3 (Fig. 5e). Therefore, the d-band center of WO_{3-x} is much closer to the Fermi level, indicating the electrons in W 5d orbitals of WO_{3-x} can transfer more easily and thus exhibit higher catalytic ability [53,54].

In Fig. 5f, it is clear that the electrons of WO_{3-x} present obvious spin polarization state (especially above the Fermi level), which can be attributed to the introduction of OVs. The electrons with spin polarization state will retard the recombination of photogenerated h^+–e^- pairs during the charge transfer process. Thus, for WO_{3-x}, after a spin-down electron is photoexcited to conduction band (mainly W 5d orbitals),

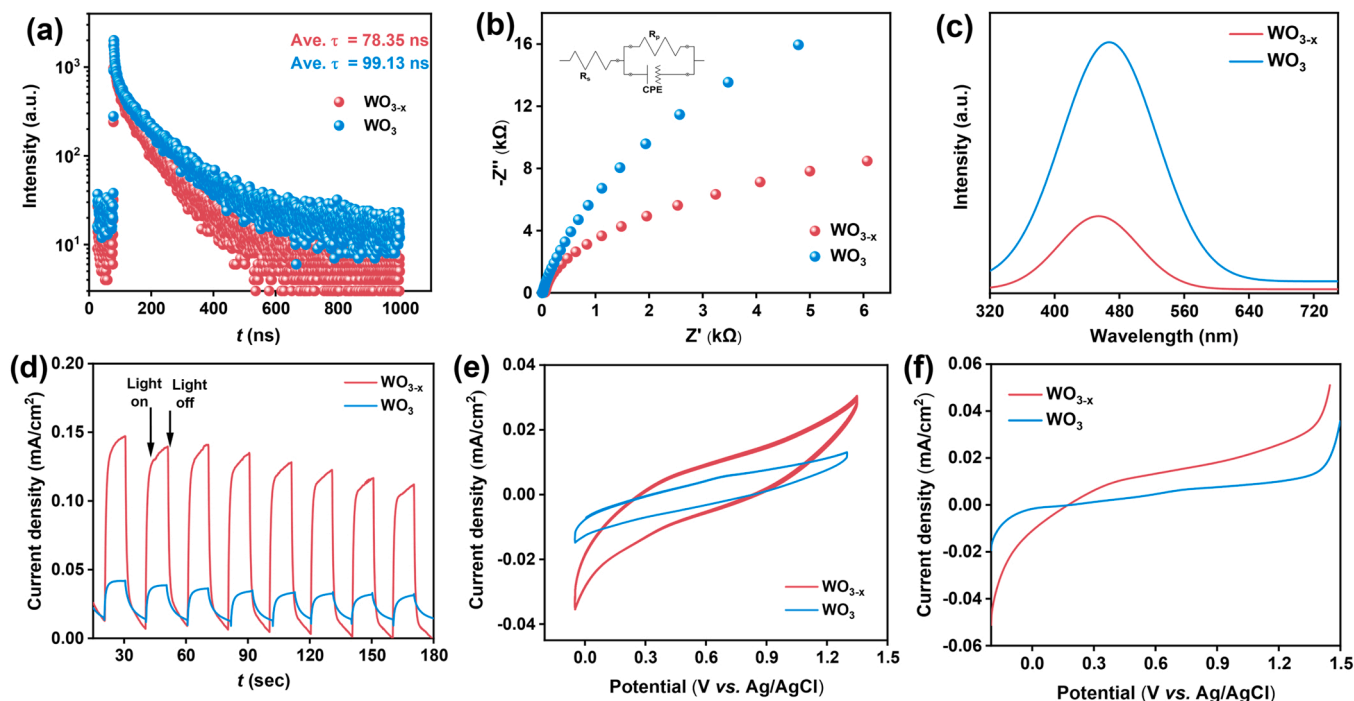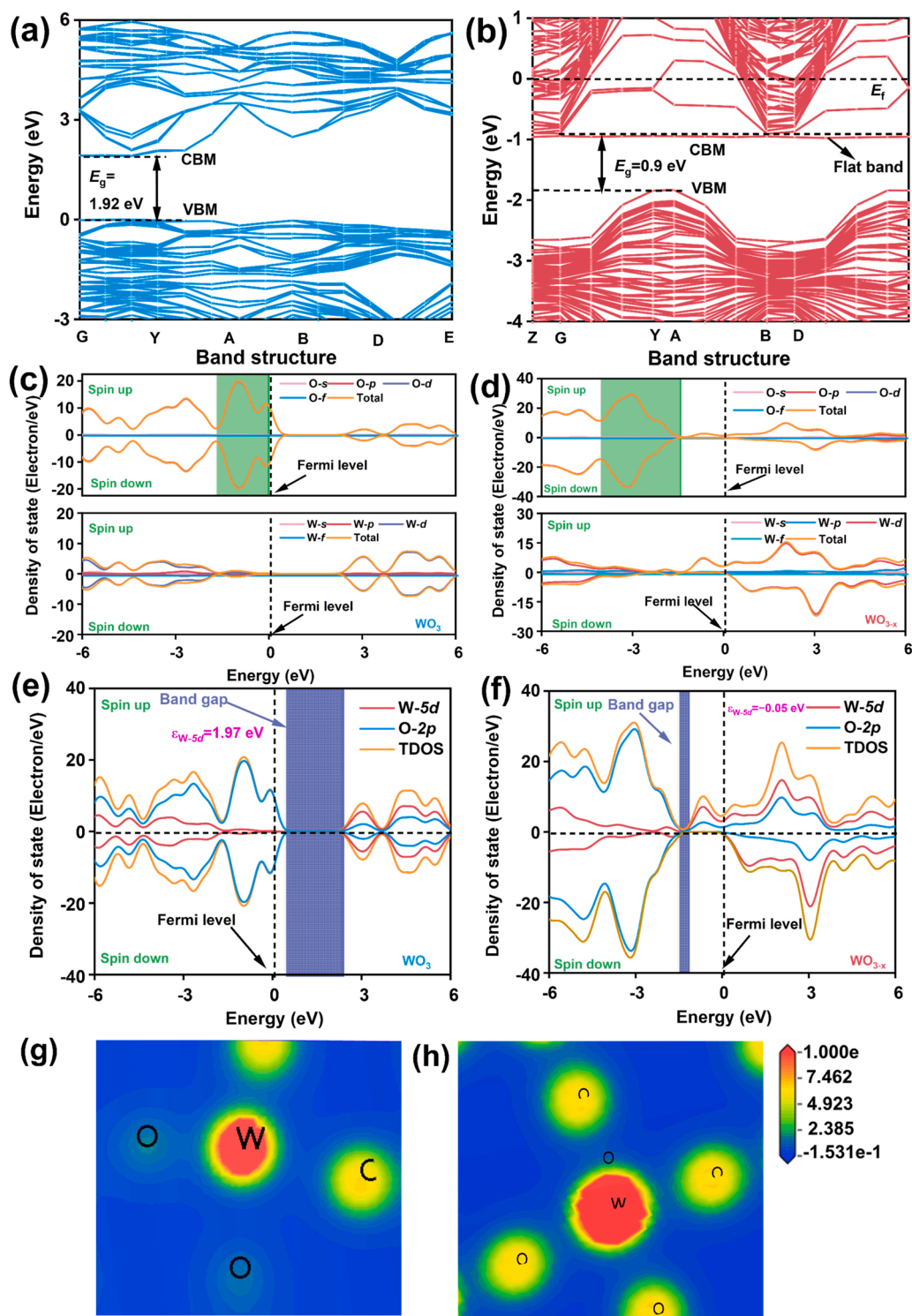**Fig. 4.** (a) TR-PL spectra, (b) EIS, (c) PL spectra, (d) photocurrent (*i-t* curve), (e) CV and (f) LSV of WO_{3-x} and WO_3.

Fig. 5. The calculated band structures of (a) WO$_3$ and (b) WO$_{3-x}$; PDOS spectra of (c) WO$_3$ and (d) WO$_{3-x}$; (c) DOS spectra of (e) WO$_3$ and (f) WO$_{3-x}$; electron density of (g) WO$_3$ and (h) WO$_{3-x}$.

the remaining h$^+$ in valance band (mainly O 2p orbitals) also will present the same spin-down state with spin direction unchanged. Then in the process of changer carrier transfer, the original spin direction of electrons will reverse, *i.e.*, change to spin-up state because of the spin-orbital coupling and hyperfine interaction effects. As a result, the recombination of h$^+$–e$^-$ is inhibited due to the lack of spin-up holes under the condition of high spatial spin polarization [55]. Therefore, the photocatalytic activity of WO$_{3-x}$ is promoted due to the OVs-induced

electrons spin polarization. Fig. 5g and h further display the electron density of WO$_{3-x}$ and WO$_3$, and WO$_{3-x}$ exhibits higher electron density in W 5d and O 2p, which benefits to the adsorption and reduction of U (VI). Because of electrons spin polarization in WO$_{3-x}$, the photo-generated electrons and holes can effectively separate and recombination is inhibited. Therefore, WO$_{3-x}$ shows much higher photocatalytic activity than WO$_3$, which can efficiently photocatalytic reduction of U (VI) as demonstrated in the next section.

3.4. Adsorption and photocatalytic reduction of U(VI) by WO$_{3-x}$ and WO$_3$

For adsorption kinetics of U(VI) as exhibited in Fig. 6a, both WO$_{3-x}$ and WO$_3$ could quickly capture U(VI) from solution, however, WO$_{3-x}$ exhibited much higher adsorption capacity than WO$_3$. Specifically, the adsorption of U(VI) on WO$_{3-x}$ mainly occurred in the initial 30 min, and then quickly reached adsorption equilibrium within 180 min. The equilibrium adsorption capacity (q_e) of U(VI) on WO$_{3-x}$ was 287.1 mg/g, which was ~14 time of that on WO$_3$ (only 20.5 mg/g). The *pseudo*-first and *pseudo*-second order kinetic models (Text S5) were further applied to describe the kinetics data of U(VI) adsorption [38]. Table S7 indicates that the *pseudo*-second order model ($R^2 = 0.993$ for WO$_{3-x}$ and 0.996 for WO$_3$) could well fit the kinetics data, and the calculated q_e values (282.6 mg/g for WO$_{3-x}$ and 20.6 mg/g for WO$_3$) *via* model were close to the experimental capacities (287.1 mg/g for WO$_{3-x}$ and 20.5 mg/g for WO$_3$). Therefore, the adsorption U(VI) by WO$_3$ and WO$_{3-x}$ was a chemical-control reaction process and surface complexation (interaction between W–O bond and UO$_2^{2+}$) was the primary mechanism [56].

Adsorption isotherms results further demonstrated the excellent adsorption performance of WO$_{3-x}$ for U(VI) (Fig. S4). Two classical adsorption isotherm models, *i.e.* Langmuir and Freundlich were introduced to describe the isotherm data (Text S5) [57]. Table S8 indicates that the Langmuir model showed a better fit on the experimental result ($R^2 = 0.974$), with a U(VI) maximum adsorption capacity (Q_{max}) of 337.0 mg/g for WO$_{3-x}$, indicating that the adsorption process belonged to the manner of monolayer adsorption [3]. In comparison, WO$_3$ only presented weak adsorption ability to U(VI) with Q_{max} of 24.3 mg/g. The separation factor (R_L), which is a dimensionless constant to describe adsorption affinity (Eq. S7 in Text S5), and $0 < R_L < 1$ indicates favorable adsorption [58]. The R_L value was calculated as 0.15 at $C_0 = 50$ mg/L and 0.08 at $C_0 = 100$ mg/L of U(VI), suggesting the U(VI) adsorption onto WO$_{3-x}$ was extremely favorable. Thus, the introduction of OVs in WO$_{3-x}$ and the specific nanowire structure with large BET surface area dramatically promoted the adsorption capability of WO$_{3-x}$ [41]. The underlying mechanism on U(VI) adsorption by WO$_{3-x}$ and the high affinity will be discussed in Section 3.6 in detail.

Fig. 6b presents photocatalytic reduction of U(VI) and formation of U(IV) along time, which were evaluated after CARB extraction. The concentration of U(VI) was almost unchanged under simulated solar light without catalysts addition. In addition, WO$_3$ exhibited a low removal efficiency (14.9%) of U(VI), in which only 9.6% was reduced to U(IV) after 4 h light irradiation. In comparison, WO$_{3-x}$ had superior advantage to achieve efficient U(VI) reduction. As high as 79.9% of U(VI) was efficiently reduced to U(IV) after 4 h light irradiation and the total U removal efficiency was up to 95.1%. The first order kinetic model was further applied to obtain the rate constant (k_1) for U(VI) photocatalytic reduction (Eq. 8 in Text S5) [59]. The k_1 value for WO$_{3-x}$ (0.44 h^{-1}) was ~22 times of that for WO$_3$ (0.02 h^{-1}), verifying the much better photocatalytic property of WO$_{3-x}$ with OVs.

Methanol, a conventional hole quenching agent, was added to evaluate the separation efficiency of e^-–h$^+$ pairs for WO$_{3-x}$ and WO$_3$ during photocatalytic reduction of U(VI) [54]. Fig. S5 shows the reduction rate of U(VI) by WO$_{3-x}$ was almost did not change after methanol addition, demonstrating that efficient e^-–h$^+$ separation was achieved for WO$_{3-x}$ even if no hole quenching agent was added. However, the addition of methanol greatly increased the U(VI) reduction efficiency from 9.6% to 37.8%, suggesting the low e^-–h$^+$ separation efficiency for WO$_3$. EPR analysis was applied to identify the produced radicals including •OH and •O$_2^-$ during photocatalysis. Fig. S6 displays that the signal of DMPO-•OH ($\alpha_N = \alpha_H = 14.9$ G with peak intensity of 1:2:2:1) [60] was observed in the WO$_{3-x}$ photocatalysis system, which is in agreement with the higher oxidation potential of VB (2.44 eV *vs* NHE) than H$_2$O/•OH (2.34 eV) and H$_2$O/•OH (1.99 eV) [61]. No DMPO-•O$_2^-$ signal was found even under light irradiation, as the CB value (–0.10 eV) of WO$_{3-x}$ was less negative than that of O$_2$/•O$_2^-$ (–0.33 eV) [62]. Therefore, the U(VI) reduction by WO$_{3-x}$ was mainly attributed to the
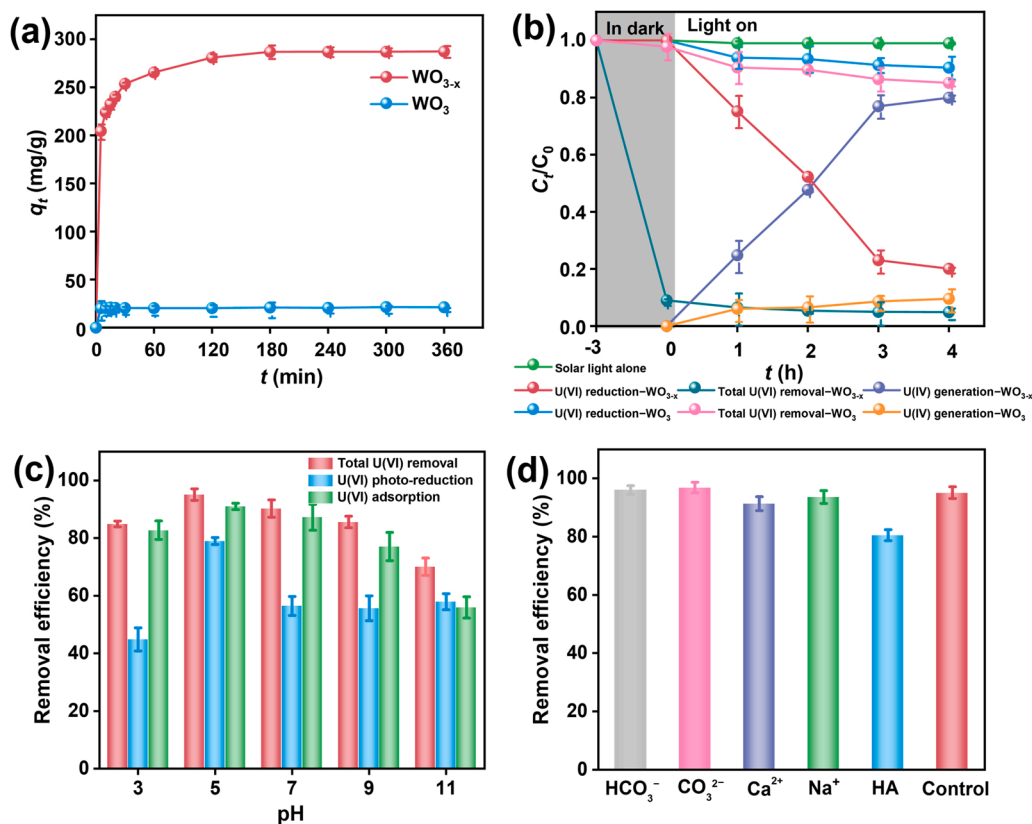
Fig. 6. (a) Adsorption kinetics of U(VI) by WO$_{3-x}$ and WO$_3$; (b) photocatalytic removal of U(VI) and formation of U(IV) by WO$_{3-x}$ and WO$_3$ under simulated solar light; (c) effect of pH on U(VI) adsorption and photocatalytic reduction by WO$_{3-x}$; (d) effect of coexisting ions and HA on U(VI) removal by WO$_{3-x}$ under simulated solar light. (Experimental conditions: catalyst dosage = 0.2 g/L, pH = 5 ± 0.1 for (a), (b) and (d); for (a), initial U(VI) concentration = 100 mg/L; for (b), (c) and (d), initial U (VI) = 10 mg/L, solar light intensity = 80 ± 5 mW/cm^2; for (d), ions concentration = 5 mM, HA = 5 mg/L.).

photogenerated e^- at CB but not reducing species such as $\bullet O_2^-$. The signal intensity of DMPO-$\bullet$OH was weaker and no DMPO-$\bullet O_2^-$ was identified for WO_3, due to its low photocatalytic activity. In addition, O_2 also may be generated in the photocatalysis process *via* a series of radical chain reaction [63]. Thus, in this system, the generation of O_2 also was detected by gas chromatography (GC) (detailed method presented in Text S6). It clearly can be observed that no apparent O_2 peak was found within 6 h under the simulated solar light (Fig. S7), indicating that the generation of O_2 could be ignored and the photo-oxidation product was mainly $\bullet$OH.

3.5. Effects of pH and coexisting ions on removal of U(VI) by WO_{3-x}

pH generally plays an important role in both adsorption and photocatalysis of U(VI) [5]. Fig. S8 presents the speciation of U(VI) as a function of pH [3]. Fig. 6c indicates the optimized pH was 5–7 for U(VI) adsorption. It is because U(VI) mainly existed in the form of metal cations at pH ≤ 7, such as UO_2^{2+}, $(UO_2)_2(OH)_2^{2+}$, $(UO_2)_3(OH)_5^+$ $(UO_2)_4(OH)^{7+}$ (Fig. S8), so adsorption was promoted when more negative charges on the surface of WO_{3-x} with increasing pH (Fig. S9). However, at ≥ 7, U(VI) species were primly metal anions including $(UO_2)_3(OH)_7^-$, $UO_2(OH)_3^-$ and $UO_2(OH)_4^{2-}$, so adsorption was inhibited with increasing pH due to electrostatic repulsion [57,64]. For U(VI) photocatalysis, the presence of H^+ facilitated U(VI) reduction according to Eq. 10 (shown in Section 3.6) [64], so higher photo-reduction efficiency was obtained at acidic condition (pH 5). The low adsorption capacity of U(VI) at pH 3 inhibited the further reduction reaction at the interface of material. Moreover, tungsten oxides are generally unstable and will decompose into WO_4^{2-} at alkaline condition [40], also leading to the low adsorption capacity and photocatalytic activity at higher pH. Therefore, the best U(VI) removal efficiency (95.1%) was obtained at pH 5. Moreover, the highest adsorption efficiency (91.0%) and highest photocatalytic reduction efficiency (79.9%) of U(VI) were also obtained at pH 5.

Various ions (*e.g.*, HCO_3^-, CO_3^{2-}, Ca^{2+}, Na^+) and NOM (*e.g.*, humic acid, HA) widely exist in the real U(VI) wastewaters, which bring non-negligible impacts on U(VI) removal [65]. However, Fig. 6d shows the developed WO_{3-x} in this study still exhibited high removal efficiencies for U(VI) removal (all >90%) with the coexistence of various ions, indicating the high stability and good performance of WO_{3-x}. Specifically, the presence of Ca^{2+} decreased the U(VI) removal efficiency from 95.1% to 91.3%, because Ca^{2+} possessed stronger double-layer compression effect on material and competition effect for adsorption sites with UO_2^{2+}, thus inhibiting the interfacial reaction [66]. In addition, Ca^{2+} also can complex with UO_2^{2+} in the presence of CO_3^{2-}/HCO_3 in air according to Eqs. 4 and 5, further inhibiting the removal efficiency during the photocatalytic process [67]. The presence of HA inhibited the U(VI) removal by 14.6%, because: (1) HA would coated on the surface of material, thus preventing the interaction between WO_{3-x} and UO_2^{2+} [10]; and (2) HA could combine with U(VI) to form binary $UO_2HA(II)$ and ternary $UO_2(OH)HA(I)$ complexes, thus reducing the adsorption of U(VI) and further reaction [67].

$$UO_2^{2+} + Ca^{2+} + 3CO_3^{2-} = CaUO_2(CO_3)_3^{2-} \tag{4}$$

$$UO_2^{2+} + 2Ca^{2+} + 3CO_3^{2-} = CaUO_2(CO_3)_3 \text{ (aq)} \tag{5}$$
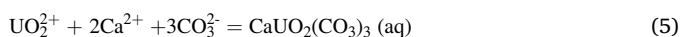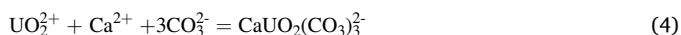
The reusability and stability of WO_{3-x} during photocatalysis under simulated solar light were also evaluated. After five reuse cycles, the total U(VI) removal efficiency also could reach up to 88.8% (Fig. S10a). In addition, only 4.43% of W was leached into solution over five cycles (Fig. S10b), suggesting the good stability of WO_{3-x}. Therefore, the developed WO_{3-x} has great practical application potential for U-contaminated water treatment. The wavelength-dependent experiments were also conducted to explore the contribution of lights with different wavelengths. Fig. S11 shows 40.5% of U(VI) ($k_1 = 0.13 \text{ h}^{-1}$) was reduced when UV light was cut off, while 22.2% of U(VI) ($k_1 =$

0.060 h^{-1}) was reduced under NIR light. Then, for the 79.9% of U(VI) reduction under solar light, the contributions of different lights were calculated as: UV light (39.4%) > NIR light (22.2%) > visible light (18.3%). High UV region contribution was due to the strong adsorption at this region (Fig. 3a), and high NIR region contribution resulted from the LSPR effect of WO_{3-x}.

3.6. The mechanism of enhanced U removal by WO_{3-x} and role of OVs

To explore the composition and bonding of U after adsorption and photo-reduction, the XPS spectra of WO_{3-x} after reaction with U loading are presented in Fig. 7. In the survey spectra of WO_{3-x} (Fig. 7a), it is clear that the U 4 f peak emerged after adsorption and photocatalytic reduction. In the high-resolution spectra of W 4 f (Fig. 7b), the peaks of W(VI) and W(V) slightly shifted to high binding energies after adsorption. However, both of the peaks dramatically shifted to lower binding energies after photo-reduction, *i.e.*, from 36.1 to 35.7 eV for W(VI) and from 34.7 to 34.4 eV for W(V), respectively. In addition, XPS analysis of WO_{3-x} after solar light irradiation without UO_2^{2+} addition was conducted to evaluate if self-reduction of WO_{3-x} occurred. Fig. S12 displays that the binding energy of W 4 $f_{7/2}$ peaks for WO_{3-x} changed by 0.3 eV and 0.2 eV for W(VI) and W(V) after solar light irradiation, respectively. However, Fig. 7b presents W 4 $f_{7/2}$ peaks further shifted by 0.4 eV and 0.3 eV of W(VI) and W(V) after photo-reduction (from 36.1 eV to 35.7 eV and 34.7–34.4 eV of WO_{3-x} for adsorbing UO_2^{2+}), respectively, indicating the introduction of UO_2^{2+} also caused the alteration of W 4 f peaks due to interaction of UO_2^{2+} with WO_{3-x}. Therefore, it is indicated that W in WO_{3-x} participated in photocatalytic reaction [68], which is consistent with the DFT calculation results in Section 3.3. In the high-resolution spectra of O 1 s (Fig. 7c), the percentage of O_A peak altered from 15.80% to 30.48% after U(VI) adsorption due to the adsorption of hydroxylated uranyl ions such as $(UO_2)_3(OH)_5^+$, $(UO_2)_2(OH)_2^{2+}$ and $(UO_2)_4(OH)_7^+$. Besides, the percentage of O_V peak also increased from 24.05% to 32.99% after adsorption, attributed to the existence of unsaturated U=O groups of adsorbed uranyl ions [69]. After photo-reduction, the percentage of O_L peak increased from 36.53% to 45.16%, owing to the decomposition of adsorbed hydroxylated U(VI) ions and the formation of UO_2 (solid, O in the form of O_L). In the high resolution spectra of U 4 f (Fig. 7d), the peaks at 382.2 and 380.1 eV in U 4 $f_{7/2}$ belonged to U(VI) and U(IV), respectively [70]. No peak assigned to U(IV) was observed after adsorption, indicating no transformation of U species during the adsorption. However, an obvious peak attributed to U(IV) was formed after photocatalysis, which accounted for 75.13% of total U, which was consistent with the experimental value of 79.9% reduction efficiency, suggesting successful photocatalytic reduction of U (VI) to U(IV) under solar light.

Generally, for the heterogenous reaction such as photocatalysis of U (VI) by WO_{3-x}, the first step is adsorption of U(VI) onto the specific lattice structure of material, then interfacial reaction proceeds for converting of U(VI) to U(IV) *via* photocatalysis [56]. To reveal the high affinity of WO_{3-x} to U(VI), as well as the role of OVs in interfacial interaction with U(VI), theoretical calculations on U(VI) adsorption by WO_3 and WO_{3-x} were conducted and compared (Fig. 8). At the experimental pH 5 in this study, UO_2^{2+} is the primary species of U(VI) (Fig. S7) [71], and moreover, the main exposed lattice plane was (010) for WO_{3-x}, so adsorption of U(VI) onto (010) lattice plane of material was considered for theoretical calculation. The work function results suggest WO_{3-x} ($\Phi = 3.883$ eV) can overcome less energy to transfer e^- inside the material than WO_3 ($\Phi = 5.533$ eV) (Fig. 8a and b), so WO_{3-x} exhibits more effective reduction of UO_2^{2+} under light irradiation [72], which is consistent with the TR-PL spectra and photocurrent results (Fig. 4). UO_2^{2+} mainly adsorbs on the top O atoms of (010) plane as shown in Fig. 8c and d. The distance between U and top O (in O–W) is 2.445 Å for WO_{3-x}, which is smaller than that for WO_3 (3.152 Å), indicating higher affinity of WO_{3-x} to UO_2^{2+}. Besides, WO_{3-x} also has a more negative adsorption energy ($E_{ads} = -3.87$ eV) than WO_3 ($E_{ads} = -3.27$ eV), also
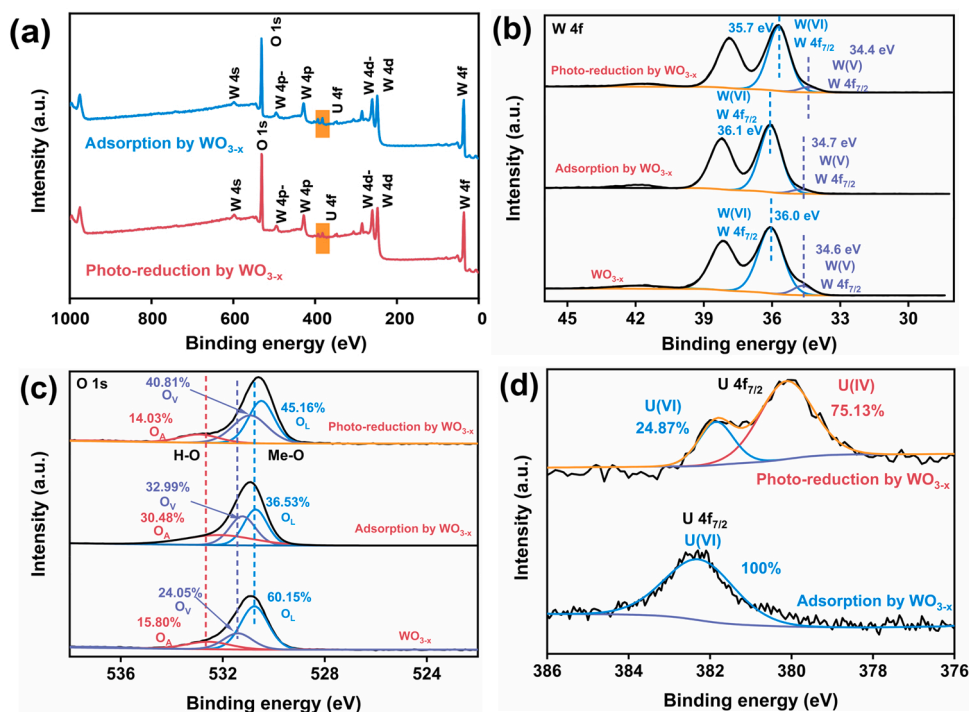
Fig. 7. XPS spectra of WO$_{3-x}$ before and after U(VI) removal: (a) survey spectra; high resolution spectra of (b) W 4 f, (c) O 1 s and (d) U 4 f.
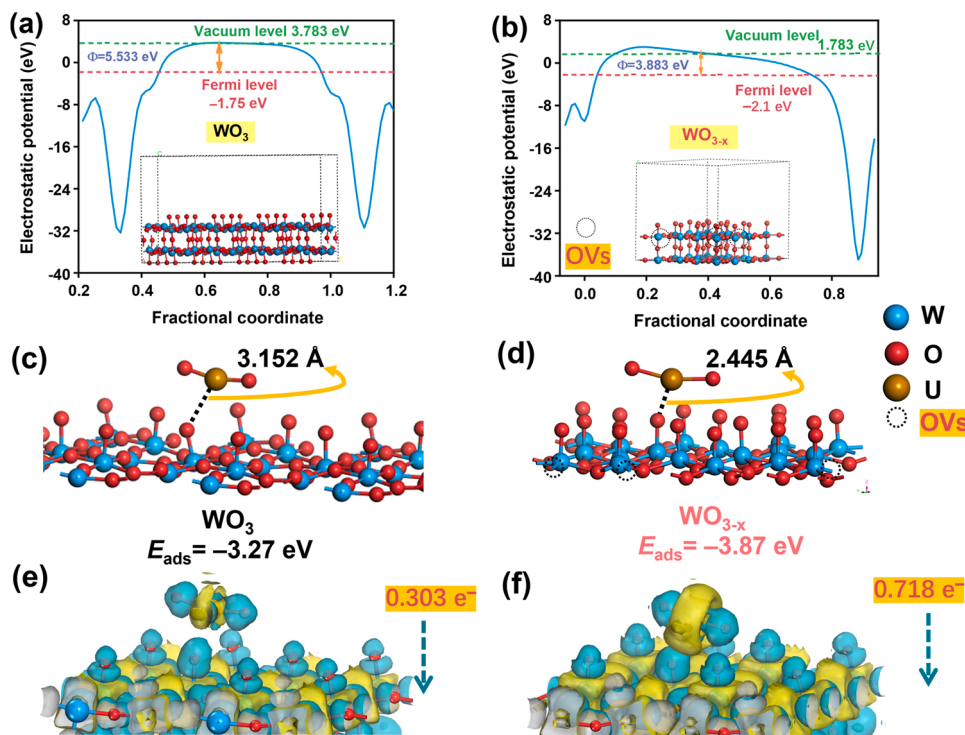

Fig. 8. The work function of (a) WO$_3$ and (b) WO$_{3-x}$; DFT calculations on adsorption of UO$_2^{2+}$ onto materials: the adsorption energy of UO$_2^{2+}$ onto (001) plane of (c) WO$_3$ and (d) (010) WO$_{3-x}$; EDD image for (001) plane of (e) WO$_3$ and (f) (010) WO$_{3-x}$ after UO$_2^{2+}$ adsorption (the isovalue is 0.05; yellow region: electrons depletion; cyan region: electrons accumulation).

confirming the stronger adsorption ability of UO$_2^{2+}$ by WO$_{3-x}$. Furthermore, EDD is analyzed to reveal the charge distribution and transfer direction after UO$_2^{2+}$ adsorption (Fig. 8e and f). Higher electron density difference between UO$_2^{2+}$ and WO$_{3-x}$ (0.718 e^-) than that of WO$_3$ (0.303 e^-) along the U–O (from O–W) direction on the surface is found, indicating WO$_{3-x}$ exhibits stronger bonding with UO$_2^{2+}$ than WO$_3$ [73].

To prove the main reason for the improved photocatalytic activity is oxygen vacancy-induced spin polarization instead of increased specific surface area. A WO$_{3-x}$ with low OVs concentration (L-WO$_{3-x}$) was prepared at a lower temperature (160 °C) based on the previous study [26]. The EPR spectra in Fig. 9a confirm the lower OVs concertation of L-WO$_{3-x}$ compared with WO$_{3-x}$ due to the weaker signal intensity at *g*
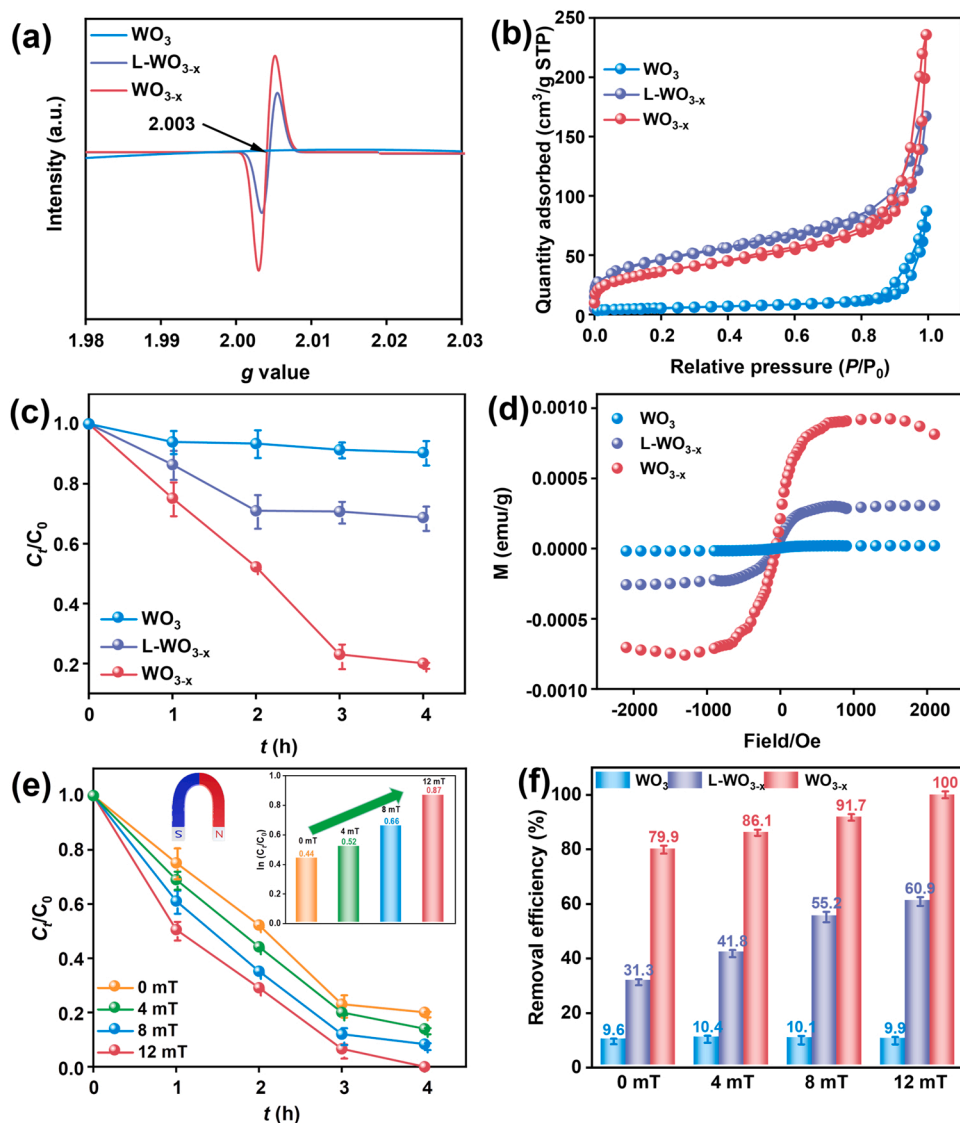
Fig. 9. (a) EPR spectra and (b) N_2 adsorption-desorption curves of WO_3, $L-WO_{3-x}$ and WO_{3-x}; (c) U(VI) reduction kinetics by using different materials; (d) the magnetization (M-H) curves of WO_{3-x} and WO_3 at 400 K; (e) U(VI) reduction kinetics by WO_{3-x} after the introduction of magnetic field; (f) U(VI) reduction efficiencies by using different materials after the introduction of magnetic field. (Experimental conditions: catalyst dosage = 0.2 g/L, pH = 5 ± 0.1, initial U(VI) = 10 mg/L, solar light intensity = 80 ± 5 mW/cm^2, applied magnetic field = 0–12 mT).

= 2.003. Fig. 9b indicates the specific surface area of $L-WO_{3-x}$ (112.5 m^2/g) was just slightly smaller than that of WO_{3-x} (123.6 m^2/g), but much larger than that of WO_3 (18.6 m^2/g). In addition, the band gap energy (E_g = 2.58 eV, light absorption edge of 480 nm) of $L-WO_{3-x}$ was also similar to that of WO_{3-x} (E_g = 2.54 eV, light absorption edge of 488 nm) (Fig. S13). However, Fig. 9c shows that $L-WO_{3-x}$ exhibited only 31.3% of U(VI) reduction efficiency at 4 h after photocatalysis, which was much lower than 79.9% for WO_{3-x}. It is indicated that the specific surface area and band gap energy were not the key factors for photocatalytic activity of WO_{3-x} with different OVs concentrations, and OVs-induced the spin polarization played a more important role. Fig. 9d displays WO_{3-x} possessed stronger saturation magnetization signal than WO_3 and $L-WO_{3-x}$, suggesting that WO_{3-x} with single electron existed significant spin polarization [55,74]. Moreover, the enhanced photocatalytic performance owing to spin polarization was further verified by introduction of applied magnetic field. Fig. 9e displays the U(VI) reduction efficiency by using WO_{3-x} gradually increased from 79.9% to 100% when the magnetic field strength enhanced from 0 to 12 mT, as the k_1 value also increased from 0.44 to 0.87 h^{-1}. The U(VI) reduction efficiency by using $L-WO_{3-x}$ also increased from 31.3% to 60.9% due to spin polarization effect (Fig. 9f). However, the removal efficiency of U(VI) by WO_3 without OVs was almost unchanged under the applied magnetic field (Fig. 9f), indicating that the OVs-induced spin

polarization of WO_{3-x} exactly led to promoted photocatalytic performance. Thus, the above results have verified the spin polarization caused by OVs is the key mechanism for the photocatalytic activity enhancement, consistent with DFT calculation results (Fig. 5).

Fig. 10 summarizes the schematic diagram on removal of U(VI) by WO_{3-x} through adsorption and photocatalytic reduction. The U(VI) species (mainly UO_2^{2+}) will firstly adsorb onto WO_{3-x} through complexation (Eq. (6)). Afterwards, under simulated solar light irradiation, the material will capture photons for production of electrons (e^-, CB), and the remaining part is hole (h^+, VB) (Eq. (7)). Meanwhile, the h^+ will keep opposite direction compared with e^- due to the spin polarization of WO_{3-x}, thus preventing the recombination of e^-–h^+ pairs [24]. Then, h^+ will react with OH$^-$/H_2O to produce •OH (Eq. (8)). The photogenerated e^- will transfer to CB, and then reduce the adsorbed U(VI) to generate U(VI) species (mainly UO_2) (Eqs. (9)–(10)). Meanwhile, the CB also can produce hot electrons to participate in photo-reduction process due to the LSPR effect caused by OVs [45]. As the measured CB of WO_{3-x} is – 0.10 eV *vs.* NHE for WO_{3-x}, which is more negative than the U(VI) reduction potential (*i.e.* 0.411 V for UO_2^{2+}/UO_2 and 0.267 V for UO_2^{2+}/U^{4+}), so photocatalytic reduction of U(VI) can occur on WO_{3-x} (Fig. 3e). In total, the roles of OVs in enhanced photocatalytic reduction of U(VI) by WO_{3-x} can be summered as: (1) OVs lead to spin polarization of electrons in WO_{3-x}, thus inhibiting the recombination of
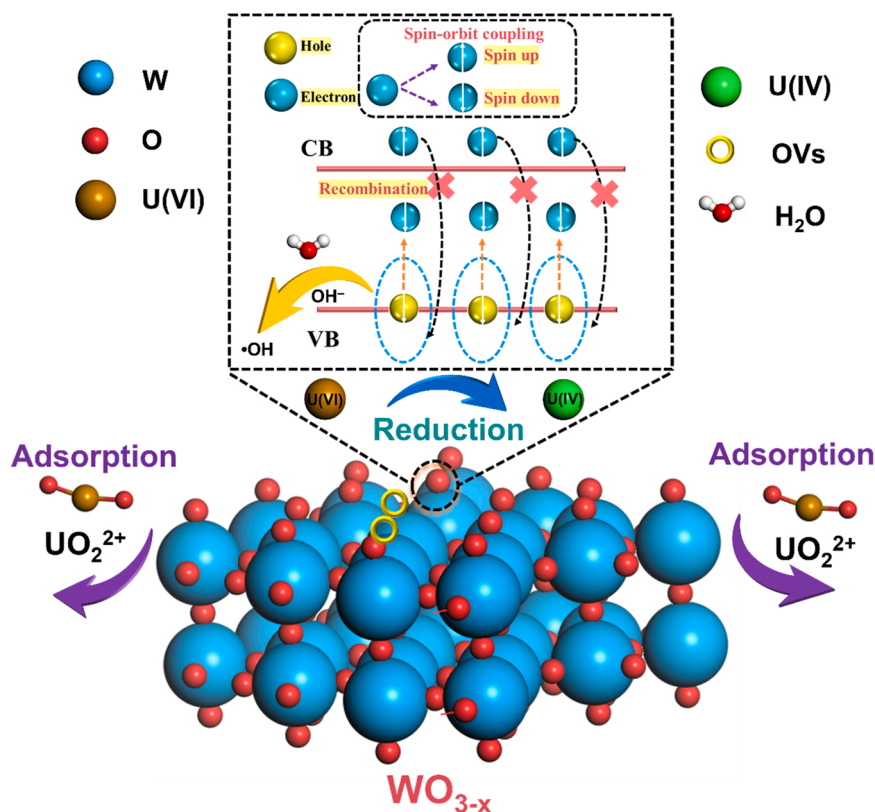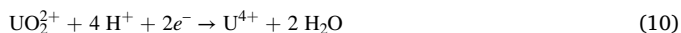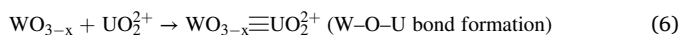
Fig. 10. The schematic diagram on removal of U(VI) by WO_{3-x} through adsorption and photocatalytic reduction.

photogenerated e^- and h^+; (2) OVs regulate the band structure of material, *i.e.*, narrowed band gap and generation of defect level, facilitating the light absorption in visible and NIR regions; (3) OVs modulate the electron state near the Fermi level, so the d-band center of W 5d (mainly contributed to CB) is closer to Fermi level, leading to high adsorption affinity to UO_2^{2+} and high reactivity of d-band electron.

$$WO_{3-x} + UO_2^{2+} \rightarrow WO_{3-x}\equiv UO_2^{2+} \text{ (W–O–U bond formation)} \qquad (6)$$

$$WO_{3-x} + hv \rightarrow e^- + h^+ \text{ (excitation)} \qquad (7)$$

$$h^+ + OH^-/H_2O \rightarrow \bullet OH + H^+ \qquad (8)$$

$$UO_2^{2+} + 2e^- \rightarrow UO_2 \text{ (s)} \qquad (9)$$

$$UO_2^{2+} + 4\,H^+ + 2e^- \rightarrow U^{4+} + 2\,H_2O \qquad (10)$$

4. Conclusions

In this study, WO_{3-x} with rich OVs was fabricated by a simple solvothermal method, which exhibited both high adsorptive performance and photocatalytic activity. Thus, efficient removal of U(VI) through initial adsorption and subsequent reduction was obtained by using WO_{3-x} under simulated solar light. Specifically, 95.1% of total U(VI) could be removed and 79.9% was reduced to U(IV) at pH 5. WO_{3-x} exhibited a large monolayer adsorption capacity (Q_{max}) of 337.0 mg/g for U(VI), which was ~14 times of conventional WO_3 ($Q_{max} = 24.3$ mg/g). In addition, WO_{3-x} showed high first order rate constant for U(VI) photocatalytic reduction ($k_1 = 0.44$ h^{-1}), which was ~22 times of WO_3 ($k_1 = 0.02$ h^{-1}). Moreover, high U(VI) removal efficiencies were also found at wide pH ranges and even with the coexistence of ions/NOM. The enhanced adsorptive and photocatalytic properties are mainly ascribed to the construction of OVs. The promoted adsorption performance of WO_{3-x} is mainly attributed to: (1) WO_{3-x} presents as nanowire structure with large specific surface area by introducing OVs, thus possessing abundant adsorption sites for U(VI); (2) the d-band center of W 5d is closer to Fermi level due to construction of OVs, leading to high adsorption affinity to UO_2^{2+} by WO_{3-x}. The enhanced photocatalytic activity of WO_{3-x} is mainly attributed to: (1) OVs lead to spin polarization of electrons in WO_{3-x}, thus inhibiting the recombination of photogenerated e^- and h^+; (2) OVs regulate the band structure of material, *i.e.*, narrowed band gap and generation of defect level, facilitating the light absorption and photogenerated charge carrier transfer; (3) OVs modulate the electron state near the Fermi level, thus promoting the reactivity of electron in W 5d band. This study can explore the mechanism on promoted adsorptive and photocatalytic properties of tungsten oxide by introducing of OVs, and also can present efficient technologies for treatment of U(VI)-contaminated wastewaters through green photocatalysis.

CRediT authorship contribution statement

Xudong Yang: Conceptualization, Methodology, Investigation, Software-DFT calculation, Writing – original draft. **Fan Li:** Conceptualization, Software-DFT calculation. **Wen Liu:** Resources, Conceptualization, Writing – review & editing, Supervision, Funding acquisition. **Long Chen:** Investigation, Validation. **Juanjuan Qi:** Investigation, Validation. **Weiliang Sun:** Investigation, Validation, Software-DFT calculation. **Fei Pan:** Validation, Writing – review & editing. **Tao Duan:** Writing – review & editing, Funding acquisition. **Fengbin Sun:** Resources, Supervision, Funding acquisition.

Declaration of Competing Interest

The authors declare that they have no known competing financial interests or personal relationships that could have appeared to influence the work reported in this paper.

Data availability

Data will be made available on request.

Appendix A. Supporting information

Supplementary data associated with this article can be found in the online version at doi:10.1016/j.apcatb.2022.122202.

References

[1] Z.J. Li, Z.W. Huang, W.L. Guo, L. Wang, L.R. Zheng, Z.F. Chai, W.Q. Shi, Enhanced photocatalytic removal of uranium(VI) from aqueous solution by magnetic TiO$_2$/Fe$_3$O$_4$ and its graphene composite, Environ. Sci. Technol. 51 (2017) 5666–5674.

[2] F. Yu, Z. Zhu, S. Wang, J. Wang, Z. Xu, F. Song, Z. Dong, Z. Zhang, Novel donor-acceptor-acceptor ternary conjugated microporous polymers with boosting forward charge separation and suppressing backward charge recombination for photocatalytic reduction of uranium(VI), Appl. Catal. B 301 (2022), 120819.

[3] X. Liu, P. Du, W. Pan, C. Dang, T. Qian, H. Liu, W. Liu, D. Zhao, Immobilization of uranium(VI) by niobate/titanate nanoflakes heterojunction through combined adsorption and solar-light-driven photocatalytic reduction, Appl. Catal. B 231 (2018) 11–22.

[4] X.-H. Jiang, Q.-J. Xing, X.-B. Luo, F. Li, J.-P. Zou, S.-S. Liu, X. Li, X.-K. Wang, Simultaneous photoreduction of uranium(VI) and photooxidation of arsenic(III) in aqueous solution over g-C$_3$N$_4$/TiO$_2$ heterostructured catalysts under simulated sunlight irradiation, Appl. Catal. B 228 (2018) 29–38.

[5] X. Nie, Y. Zhang, Y. Jiang, N. Pan, C. Liu, J. Wang, C. Ma, X. Xia, M. Liu, H. Zhang, X. Li, F. Dong, Efficient extraction of U(VI) from uranium enrichment process wastewater by amine-aminophosphonate-modified polyacrylonitrile fibers, Sci. Total Environ. 831 (2022) 154743.

[6] J. Lei, H. Liu, C. Yuan, Q. Chen, J.A. Liu, F. Wen, X. Jiang, W. Deng, X. Cui, T. Duan, W. Zhu, R. He, Enhanced photoreduction of U(VI) on WO$_3$ nanosheets by oxygen defect engineering, Chem. Eng. J. 416 (2021), 129164.

[7] M.L. Feng, D. Sarma, X.H. Qi, K.Z. Du, X.Y. Huang, M.G. Kanatzidis, Efficient removal and recovery of uranium by a layered organic-inorganic hybrid thiostannate, J. Am. Chem. Soc. 138 (2016) 12578–12585.

[8] S. Singh, M. Kaur, B.S. Bajwa, I. Kaur, Salicylaldehyde and 3-hydroxybenzoic acid grafted NH$_2$-MCM-41: Synthesis, characterization and application as U(VI) scavenging adsorbents using batch mode, column and membrane systems, J. Mol. Liq. 346 (2022), 117061.

[9] E. Ansoborlo, L. Lebaron-Jacobs, O. Prat, Uranium in drinking-water: A unique case of guideline value increases and discrepancies between chemical and radiochemical guidelines, Environ. Int. 77 (2015) 1–4.

[10] E. Liger, L. Charlet, P. Van, Cappellen, Surface catalysis of uranium(VI) reduction by iron(II), Geochim. Cosmochim. Acta 63 (1999) 2939–2955.

[11] Y. Xie, Q. Fang, M. Li, S. Wang, Y. Luo, X. Wu, J. Lv, W. Tan, H. Wang, K. Tan, Low concentration of Fe(II) to enhance the precipitation of U(VI) under neutral oxygen-rich conditions, Sci. Total Environ. 711 (2020), 134827.

[12] P.-L. Liang, L.-Y. Yuan, H. Deng, X.-C. Wang, L. Wang, Z.-J. Li, S.-Z. Luo, W.-Q. Shi, Photocatalytic reduction of uranium(VI) by magnetic ZnFe$_2$O$_4$ under visible light, Appl. Catal. B 267 (2020) 118688.

[13] X. Yang, J. Duan, X. Zhang, H. Zhang, X. Liu, Y. Feng, M. Zheng, Heterojunction architecture of Nb$_2$O$_5$/g-C$_3$N$_4$ for enhancing photocatalytic activity to degrade organic pollutants and deactivate bacteria in water, Chin. Chem. Lett. 33 (2022) 3792–3796.

[14] X.-Y. Zhang, J.-J. Wang, P. Li, Z.-Y. Tan, J.-H. Zeng, Y.-R. He, N. Habibul, Removal of U(VI) from aqueous solution via photocatalytic reduction over WO$_3$/g-C$_3$N$_4$ composite under visible light, Chem. Eng. J. 428 (2022), 131209.

[15] T. Chen, P. He, T. Liu, L. Zhou, M. Li, K. Yu, Q. Meng, J. Lian, W. Zhu, MXene-derived 3D defect-Rich TiO$_2$@reduced graphene oxide aerogel with ultrafast carrier separation for photo-assisted uranium extraction: A combined batch, X-ray absorption spectroscopy, and density functional theory calculations, Inorg. Chem. 61 (2022) 12759–12771.

[16] H. Deng, Z. Li, L. Wang, L. Yuan, J. Lan, Z. Chang, Z. Chai, W. Shi, Nanolayered Ti$_3$C$_2$ and SrTiO$_3$ composites for photocatalytic reduction and removal of uranium (VI), ACS Appl. Nano Mater. 2 (2019) 2283–2294.

[17] Y. Ye, J. Jin, F. Chen, D.D. Dionysiou, Y. Feng, B. Liang, H.-Y. Cheng, Z. Qin, X. Tang, H. Li, D. Yntema, C. Li, Y. Chen, Y. Wang, Removal and recovery of aqueous U(VI) by heterogeneous photocatalysis: Progress and challenges, Chem. Eng. J. 450 (2022), 138317.

[18] Y. Li, Y. Li, X. Xu, C. Ding, N. Chen, H. Ding, A. Lu, Structural disorder controlled oxygen vacancy and photocatalytic activity of spinel-type minerals: A case study of ZnFe$_2$O$_4$, Chem. Geol. 504 (2019) 276–287.

[19] W. Gao, R. Peng, Y. Yang, X. Zhao, C. Cui, X. Su, W. Qin, Y. Dai, Y. Ma, H. Liu, Y. Sang, Electron spin polarization-enhanced photoinduced charge separation in ferromagnetic ZnFe$_2$O$_4$, ACS Energy Lett. 6 (2021) 2129–2137.

[20] N. Lin, Y. Lin, X. Qian, X. Wang, W. Su, Construction of a 2D/2D WO$_3$/LaTiO$_2$N direct Z-scheme photocatalyst for enhanced CO$_2$ reduction performance under visible light, ACS Sustain. Chem. Eng. 9 (2021) 13686–13694.

[21] Y. Wang, W. Tian, C. Chen, W. Xu, L. Li, Tungsten trioxide nanostructures for photoelectrochemical water splitting: Material engineering and charge carrier dynamic manipulation, Adv. Funct. Mater. 29 (2019), 1809036.

[22] M. Ma, K. Zhang, P. Li, M.S. Jung, M.J. Jeong, J.H. Park, Dual oxygen and tungsten vacancies on a WO$_3$ photoanode for enhanced water oxidation, Angew. Chem. Int. Ed. Engl. 55 (2016) 11819–11823.

[23] Y. Liu, X. Dong, Q. Yuan, J. Liang, Y. Zhou, X. Qu, B. Dong, *In-situ* synthesis of WO$_{3-x}$/MoO$_{3-x}$ heterojunction with abundant oxygen vacancies for efficient photocatalytic reduction of CO$_2$, Colloids Surf. A 621 (2021), 126582.

[24] L. Xu, D. Gu, X. Chang, L. Chai, Z. Li, X. Jin, S. Sun, Adsorption and photocatalytic study of dye degradation over the g-C$_3$N$_4$/W$_{18}$O$_{49}$ nanocomposite, Micro Nano Lett. 13 (2018) 541–545.

[25] S. Cong, Y. Yuan, Z. Chen, J. Hou, M. Yang, Y. Su, Y. Zhang, L. Li, Q. Li, F. Geng, Z. Zhao, Noble metal-comparable SERS enhancement from semiconducting metal oxides by making oxygen vacancies, Nat. Commun. 6 (2015) 7800.

[26] M. Wang, G. Tan, S. Feng, M. Dang, Y. Wang, B. Zhang, H. Ren, L. Lv, A. Xia, W. Liu, Y. Liu, Defects and internal electric fields synergistically optimized g-C$_3$N$_{4-x}$/BiOCl/WO$_{2.92}$ heterojunction for photocatalytic NO deep oxidation, J. Hazard. Mater. 408 (2021), 124897.

[27] S.P. Hyun, J.A. Davis, K. Sun, K.F. Hayes, Uranium(VI) reduction by iron(II) monosulfide mackinawite, Environ. Sci. Technol. 46 (2012) 3369–3376.

[28] M. Segall, P.J. Lindan, Ma Probert, C. Pickard, P.J. Hasnip, S. Clark, M. Payne, First-principles simulation: Ideas, illustrations and the CASTEP Code, J. Phys. Condens. Mat. 14 (2002) 2717.

[29] Y. Zhou, Z. Wang, L. Huang, S. Zaman, K. Lei, T. Yue, Z. Li, B. You, B. Xia, Engineering 2D photocatalysts toward carbon dioxide reduction, Adv. Energy Mater. 11 (2021), 2003159.

[30] Y. Wang, X. Wang, X. Xu, T. Chen, M. Liu, F. Niu, S. Wei, J. Liu, Simultaneous synthesis of WO$_{3-x}$ quantum dots and bundle-like nanowires using a one-Pot template-free solvothermal strategy and their versatile applications, Small 13 (2017), 1603699.

[31] X. Tao, X. Pan, T. Huang, L. Chen, H. Ji, J. Qi, F. Sun, W. Liu, *In-situ* construction of Co(OH)$_2$ nanoparticles decorated urchin-like WO$_3$ for highly efficient degradation of sulfachloropyridazine via peroxymonosulfate activation: Intermediates and DFT calculation, Chem. Eng. J. 395 (2020), 125186.

[32] H. Zhang, Y. Wang, S. Zuo, W. Zhou, J. Zhang, X.W.D. Lou, Isolated cobalt centers on W$_{18}$O$_{49}$ nanowires perform as a reaction switch for efficient CO$_2$ photoreduction, J. Am. Chem. Soc. 143 (2021) 2173–2177.

[33] C. Liu, S. Mao, M. Shi, X. Hong, D. Wang, F. Wang, M. Xia, Q. Chen, Enhanced photocatalytic degradation performance of BiVO$_4$/BiOBr through combining Fermi level alteration and oxygen defect engineering, Chem. Eng. J. 449 (2022), 137757.

[34] X. Zhong, Y. Liu, W. Zeng, Y. Zhu, B. Hu, Excellent photoreduction performance of U(VI) on metal organic framework/covalent organic framework heterojunction by solar-driven, Sep. Purif. Technol. 285 (2022) 120405.

[35] W. Chen, L. Chang, S.B. Ren, Z.C. He, G.B. Huang, X.H. Liu, Direct Z-scheme 1D/2D WO$_{2.72}$/ZnIn$_2$S$_4$ hybrid photocatalysts with highly-efficient visible-light-driven photodegradation towards tetracycline hydrochloride removal, J. Hazard. Mater. 384 (2020) 121308.

[36] S.-Y. Pi, Y. Wang, C. Pu, X. Mao, G.-L. Liu, H.-M. Wu, H. Liu, Cr(VI) reduction coupled with Cr(III) adsorption/precipitation for Cr(VI) removal at near neutral pHs by polyaniline nanowires-coated polypropylene filters, J. Taiwan Inst. Chem. Eng. 123 (2021) 166–174.

[37] K. Thummavichai, L. Trimby, N. Wang, C.D. Wright, Y. Xia, Y. Zhu, Low temperature annealing improves the electrochromic and degradation behavior of tungsten oxide (WO$_x$) thin films, J. Phys. Chem. C 121 (2017) 20498–20506.

[38] Y. Shang, X. Cheng, R. Shi, Q. Ma, Y. Wang, P. Yang, Synthesis and comparative investigation of adsorption capability and photocatalytic activities of WO$_3$ and W$_{18}$O$_{49}$, Mater. Sci. Eng. B 262 (2020), 114724.

[39] B. Bhuyan, B. Paul, S.S. Dhar, S. Vadivel, Facile hydrothermal synthesis of ultrasmall W$_{18}$O$_{49}$ nanoparticles and studies of their photocatalytic activity towards degradation of methylene blue, Mater. Chem. Phys. 188 (2017) 1–7.

[40] Y. Shang, Y. Cui, R. Shi, P. Yang, J. Wang, Y. Wang, Regenerated WO$_{2.72}$ nanowires with superb fast and selective adsorption for cationic dye: Kinetics, isotherm, thermodynamics, mechanism, J. Hazard. Mater. 379 (2019), 120834.

[41] Y. Shang, Y. Cui, R. Shi, A. Zhang, Y. Wang, P. Yang, Self-reduction combined with photo-deposition decorating Au nanoparticles on urchin-like WO$_{2.72}$ for enhancement of trimethylamine-sensing performance, Mater. Sci. Semicond. Process. 101 (2019) 131–138.

[42] H. Ali, T. Vandevyvere, J. Lauwaert, S.K. Kansal, J. Saravanamurugan, J. W. Thybaut, Impact of oxygen vacancies in Ni supported mixed oxide catalysts on anisole hydrodeoxygenation, Catal. Commun. 164 (2022), 106436.

[43] H. Zeng, L. Deng, H. Zhang, C. Zhou, Z. Shi, Development of oxygen vacancies enriched CoAl hydroxide@hydroxysulfide hollow flowers for peroxymonosulfate

activation: A highly efficient singlet oxygen-dominated oxidation process for sulfamethoxazole degradation, J. Hazard. Mater. 400 (2020), 123297.

[44] X. Li, B. Kang, F. Dong, Z. Zhang, X. Luo, L. Han, J. Huang, Z. Feng, Z. Chen, J. Xu, B. Peng, Z.L. Wang, Enhanced photocatalytic degradation and H_2/H_2O_2 production performance of S-pCN/$WO_{2.72}$ S-scheme heterojunction with appropriate surface oxygen vacancies, Nano Energy 81 (2021) 10567.

[45] Y. Li, J. Wei, Z. Sun, T. Yang, Z. Liu, G. Chen, L. Zhao, Z. Cheng, Greatly enhanced photocurrent density in bismuth ferrite films by localized surface plasmon resonance effect, Appl. Surf. Sci. 583 (2022), 152571.

[46] T. Liu, Y. Wang, P. Shan, Y. Chen, X. Zhao, W. Tian, Y. Zhang, R. Feng, H. Yuan, H. Cui, Hydrogen evolution from $MoSe_2$/WO_3(001) heterojunction by photocatalytic water splitting: A density functional theory study, Appl. Surf. Sci. 564 (2021), 150117.

[47] P. Liang, L. Yuan, K. Du, L. Wang, Z. Li, H. Deng, X. Wang, S.-Z. Luo, W. Shi, Photocatalytic reduction of uranium(VI) under visible light with 2D/1D Ti_3C_2/CdS, Chem. Eng. J. 420 (2021), 129831.

[48] G. Zhang, G. Li, Z.A. Lan, L. Lin, A. Savateev, T. Heil, S. Zafeiratos, X. Wang, M. Antonietti, Optimizing optical absorption, exciton dissociation, and charge transfer of a polymeric carbon nitride with ultrahigh solar hydrogen production activity, Angew. Chem. Int. Ed. Engl. 56 (2017) 13445–13449.

[49] R. Zhu, Y. Zhu, H. Xian, L. Yan, H. Fu, G. Zhu, Y. Xi, J. Zhu, H. He, CNTs/ ferrihydrite as a highly efficient heterogeneous Fenton catalyst for the degradation of bisphenol A: The important role of CNTs in accelerating Fe(III)/Fe(II) cycling, Appl. Catal. B 270 (2020), 118891.

[50] W. Cui, J. Li, W. Cen, Y. Sun, S.C. Lee, F. Dong, Steering the interlayer energy barrier and charge flow via bioriented transportation channels in g-C_3N_4: Enhanced photocatalysis and reaction mechanism, J. Catal. 352 (2017) 351–360.

[51] F. Fungura, W.R. Lindemann, J. Shinar, R. Shinar, Carbon dangling bonds in photodegraded polymer: Fullerene solar cells, Adv. Energy Mater. 7 (2016), 1601420.

[52] Y. Qu, L. Wang, Z. Li, P. Li, Q. Zhang, Y. Lin, F. Zhou, H. Wang, Z. Yang, Y. Hu, M. Zhu, X. Zhao, X. Han, C. Wang, Q. Xu, L. Gu, J. Luo, L. Zheng, Y. Wu, Ambient synthesis of single-atom catalysts from bulk metal via trapping of atoms by surface dangling bonds, Adv. Mater. 31 (2019), 1904496.

[53] K.G. Motora, C.M. Wu, Magnetically separable highly efficient full-spectrum light-driven $WO_{2.72}$/Fe_3O_4 nanocomposites for photocatalytic reduction of carcinogeni-c chromium(VI) and organic dye degradation, J. Taiwan Inst. Chem. Eng. 117 (2020) 123–132.

[54] L. Ke, P. Li, X. Wu, S. Jiang, M. Luo, Y. Liu, Z. Le, C. Sun, S. Song, Graphene-like sulfur-doped g-C_3N_4 for photocatalytic reduction elimination of UO_2^{2+} under visible light, Appl. Catal. B 205 (2017) 319–326.

[55] L. Pan, M. Ai, C. Huang, L. Yin, X. Liu, R. Zhang, S. Wang, Z. Jiang, X. Zhang, J.-J. Zou, W. Mi, Manipulating spin polarization of titanium dioxide for efficient photocatalysis, Nat. Commun. 11 (2020) 418.

[56] W. Liu, X. Zhao, T. Wang, D. Zhao, J. Ni, Adsorption of U(VI) by multilayer titanate nanotubes: Effects of inorganic cations, carbonate and natural organic matter, Chem. Eng. J. 286 (2016) 427–435.

[57] L. Zhong, F. He, Z. Liu, B. Dong, J. Ding, Adsorption of uranium(VI) ions from aqueous solution by acrylic and diaminomaleonitrile modified cellulose, Colloids Surf. 641 (2022), 128565.

[58] K. Hall, L. Eagleton, A. Acrivos, T. Vermeulen, Pore-and solid-diffusion kinetics in fixed-bed adsorption under constant-pattern conditions, Ind. Eng. Chem. Fund. 5 (1966) 212–213.

[59] W. Liu, J. Ni, X. Yin, Synergy of photocatalysis and adsorption for simultaneous removal of Cr(VI) and Cr(III) with TiO_2 and titanate nanotubes, Water Res 53 (2014) 12–25.

[60] L. Chen, J. Duan, P. Du, W. Sun, B. Lai, W. Liu, Accurate identification of radicals by *in-situ* electron paramagnetic resonance in ultraviolet-based homogenous advanced oxidation processes, Water Res 221 (2022), 118747.

[61] F. Li, T. Huang, F. Sun, L. Chen, P. Li, F. Shao, X. Yang, W. Liu, Ferric oxide nanoclusters with low-spin Fe^{III} anchored g-C_3N_4 rod for boosting photocatalytic activity and degradation of diclofenac in water under solar light, Appl. Catal. B 317 (2022), 121725.

[62] H. Ji, P. Du, D. Zhao, S. Li, F. Sun, E.C. Duin, W. Liu, 2D/1D graphitic carbon nitride/titanate nanotubes heterostructure for efficient photocatalysis of sulfamethazine under solar light: Catalytic "hot spots" at the rutile-anatase-titanate interfaces, Appl. Catal. B 263 (2020), 118357.

[63] M. You, X. Du, X. Hou, Z. Wang, Y. Zhou, H. Ji, L. Zhang, Z. Zhang, S. Yi, D. Chen, In-situ growth of ruthenium-based nanostructure on carbon cloth for superior electrocatalytic activity towards HER and OER, Appl. Catal. B 317 (2022), 121729.

[64] X. Zhong, Y. Liu, T. Hou, Y. Zhu, B. Hu, Effect of Bi_2WO_6 nanoflowers on the U(VI) removal from water: Roles of adsorption and photoreduction, J. Environ. Chem. Eng. 10 (2022), 107170.

[65] L. Zhao, S. Wang, H. Zhuang, B. Lu, L. Sun, G. Wang, J. Qiu, Facile synthesis of low-cost $MnPO_4$ with hollow grape-like clusters for rapid removal uranium from wastewater, J. Hazard. Mater. 434 (2022), 128894.

[66] J. Qi, X. Yang, P.Y. Pan, T. Huang, X. Yang, C.C. Wang, W. Liu, Interface engineering of $Co(OH)_2$ nanosheets growing on the $KNbO_3$ perovskite based on electronic structure modulation for enhanced peroxymonosulfate activation, Environ. Sci. Technol. 56 (2022) 5200–5212.

[67] J. Duan, H. Ji, W. Liu, X. Zhao, B. Han, S. Tian, D. Zhao, Enhanced immobilization of U(VI) using a new type of FeS-modified Fe^0 core-shell particles, Chem. Eng. J. 359 (2019) 1617–1628.

[68] L. Wang, Z. Li, K. Wang, Q. Dai, C. Lei, B. Yang, Q. Zhang, L. Lei, M.K.H. Leung, Y. Hou, Tuning d-band center of tungsten carbide via Mo doping for efficient hydrogen evolution and Zn–H_2O cell over a wide pH range, Nano Energy 74 (2020), 104850.

[69] J. Huang, B. Huang, T. Jin, Z. Liu, D. Huang, Y. Qian, Electrosorption of uranium (VI) from aqueous solution by phytic acid modified chitosan: An experimental and DFT study, Sep. Purif. Technol. 284 (2022) 120284.

[70] H. Li, F. Zhai, D. Gui, X. Wang, C. Wu, D. Zhang, X. Dai, H. Deng, X. Su, J. Diwu, Z. Lin, Z. Chai, S. Wang, Powerful uranium extraction strategy with combined ligand complexation and photocatalytic reduction by postsynthetically modified photoactive metal-organic frameworks, Appl. Catal. B 254 (2019) 47–54.

[71] L.V. Moskaleva, V.A. Nasluzov, N. Rosch, Modeling adsorption of the uranyl dication on the hydroxylated α-Al_2O_3 (0001) surface in an aqueous medium: Density functional study, Langmuir 22 (2006) 2141–2145.

[72] P. Xia, S. Cao, B. Zhu, M. Liu, M. Shi, J. Yu, Y. Zhang, Designing a 0D/2D S-scheme heterojunction over polymeric carbon nitride for visible-light photocatalytic inactivation of bacteria, Angew. Chem. Int. Ed. Engl. 59 (2020) 5218–5225.

[73] W. Song, E.J.M. Hensen, Structure sensitivity in CO oxidation by a single Au atom supported on ceria, J. Phys. Chem. C 117 (2013) 7721–7726.

[74] C.-C. Lin, T.-R. Liu, S.-R. Lin, K.M. Boopathi, C.-H. Chiang, W.-Y. Tzeng, W.-H. C. Chien, H.-S. Hsu, C.-W. Luo, H.-Y. Tsai, H.-A. Chen, P.-C. Kuo, J. Shiue, J.-W. Chiou, W.-F. Pong, C.-C. Chen, C.-W. Chen, Spin-polarized photocatalytic CO_2 reduction of Mn-doped perovskite nanoplates, J. Am. Chem. Soc. 144 (2022) 15718–15726.